Rutter et al., 1988). After the buffer on the coverslip was drained, the remaining excess water was removed by filter paper. To expose the cytoplasmic surface of the upper cell membrane, the upper cell membrane was removed from the rest of the cell after it was adhered to a coverslip placed on top of the cell layer (Rutter et al., 1988; Sanan and Anderson, 1991). 5 × 5-mm coverslips (Matsunami) coated with positively charged Alcian blue 8GX (Wako; Alcian blue–coated coverslips were prepared by first immersing them in 1% Alcian blue in distilled water at room temperature for 10 min, washing them with distilled water, and drying them in the air) were placed on top of the cells (upper surface facing the medium rather than the coverslip) and incubated at 4°C for 5–15 min. During this period, good contact between the cell surface and the coverslip was developed. Then, the coverslips were gently floated off from the cell using the surface tension of the buffer by slowly adding ice-cold Pipes buffer containing 1% PFA/0.25% glutaraldehyde into the space between the culture dish and the coverslip. When the coverslip floated off, the cells were cleaved, and the upper cell membrane came off with the coverslip. Then, the cells were further fixed by incubation in fresh ice-cold 1% PFA/0.25% glutaraldehyde in Pipes buffer for 10 min. After fixation, the coverslips were washed three times, for 10 min each time, with PBS (8.10 mM Na_2HPO_4, 1.47 mM KH_2PO_4, 137 mM NaCl, and 2.68 mM KCl, pH 7.4).

To identify the actin filaments on the cytoplasmic surface of the cell membrane, immunogold labeling was performed after fixation. The fixed upper cell membranes on the coverslips with their cytoplasmic surfaces exposed toward the buffer were incubated at 4°C for 2 h in PBS containing 10 μg/ml rabbit anti-actin IgG and 1% BSA (Sigma-Aldrich), and, after three washes for 10 min each in 25 mM Tris-buffer, pH 8.0, the cell membranes were incubated in Tris-buffer containing 1% BSA and 5-nm–diameter colloidal gold conjugated with anti–rabbit IgG goat antibodies (GE Healthcare) at 4°C for 2 h. After three washes in PBS, these labeled membranes were further fixed in 2% glutaraldehyde in PBS on ice for 5 min. Finally, the coverslips were washed in distilled water for 1 min before rapid freezing.

Each coverslip was placed on the plunger tip of the rapid-freezing device (Eiko; Usukura and Yamada, 1987) with the cytoplasmic surface of the membrane facing down. The specimen was slammed down (free fall) onto a polished pure copper block, which was precooled by direct immersion in liquid helium. The frozen coverslip was placed in liquid nitrogen and was transferred into the freeze-etching shadowing chamber (FR7000-S; Hitachi). The excess ice covering the cytoplasmic surface of the membrane was shaved off with a prechilled glass knife using a microtome placed in the chamber at −140°C or below. The cytoplasmic surface was then etched for ~10 min after the specimen temperature was raised to −90°C. The etched specimen surfaces were then rotary shadowed with platinum at an angle of 22.5° from the surface and with carbon from the top. The molecules as well as the gold probes localized on the cytoplasmic surface of the cell membrane were immobilized to the deposited platinum (Fujimoto, 1995; Fujimoto et al., 1996).

Collodion was applied immediately after the platinum-carbon replicas were removed from the cold chamber to fortify them. The platinum-carbon replica was removed from the glass coverslip in 1% hydrofluoric acid in distilled water. After the replicas were successfully removed from the glass surface and mounted on the grid, the collodion coat was dissolved away in n-pentyl acetate. In this protocol, the sodium hypochlorite solution, which is generally used to remove the replicas from the coverslip and also to clear the membrane and the undercoat structure of the replicas, was replaced with 1% hydrofluoric acid to keep the cell membrane, the undercoat structure, and the immunogold probes that had been attached to these structures on the platinum replicas (1% hydrofluoric acid is likely to only dissolve the glass, leaving the cell membrane molecules bound to the platinum replica; Fujimoto, 1995; Fujimoto et al., 1996). An additional advantage of using 1% hydrofluoric acid is that the platinum replicas break less often, probably because it does not remove the membrane components and, thus, leaves the replicas rather intact. In addition, to keep as many colloidal gold particles and membrane molecules attached to the platinum replicas as possible, we included Photo-Flo 200 (Kodak), a detergent used to prevent water-drop stains on photographic film in all of the solutions used here (advice given by J. Heuser). After the replicas were washed with distilled water, they were mounted on 100–200 mesh copper grids (Ted Pella) coated with polyvinyl formvar (Nisshin EM) and observed at magnifications of ~10,000–70,000 with a transmission electron microscope (1200EX; JEOL).

The following methodological precautions and improvements were made to reproducibly produce large cell membranes and replicas without excessive fragmentation. (1) An Alcian blue coat rather than poly-L-lysine coat was used (Rutter et al., 1988; Sanan and Anderson, 1991). (2) Before overlaying the coverslips, excess water was removed from the specimen, leaving just enough buffer to cover the cell. (3) To cleave off the upper membrane attached to the overlaid coverslip, the coverslip was floated off very gently by adding cleavage medium (using the surface tension of the buffer to float the coverslip). If this was not performed gently enough, the membrane was fragmented. (4) The frozen sample was shaved with a glass knife, with the angle between the knife and the coverglass adjusted to a shallow angle (<6°) so that most of the excess water and the cytoplasm were removed and the cytoplasmic surface of the cell membrane could be exposed after light etching. Because replicas with too many variations in height tend to break when they are removed from the coverslip and placed on the water surface, removal of the excess cytoplasm helps to avoid replica breakage. (5) Collodion was applied immediately after the replicas were removed from the cold chamber (before the replicas were removed from the coverslip on the water surface) to fortify the replica (a technique learned from T. Baba and S. Ohno). This step also helped to prevent replica breakage when the replicas were removed from the coverslip. After the large replicas were removed from the glass surface, the collodion coat was dissolved away in n-pentyl acetate. (6) A solution of 1% hydrofluoric acid was used to slightly dissolve the glass surface to facilitate the removal of replicas from the coverslip. (7) A detergent, Photo-Flo 200 (Kodak), was included in all of the solutions that contacted platinum replicas.

Electron microscope tomography

For 3D reconstruction, the replica was imaged at tilt angles of every 1.0° in the range between ±48 and 70° (total of 97–141 images) for a single field by a transmission electron microscope (Tecnai Sphera F20; FEI) equipped with a CCD camera (1,024 × 1,024 pixels). The pixel size at the specimen was 0.85 nm. The image acquisition was fully automated as previously described (Medalia et al., 2002). The 100–121 image sections of every 0.85–1.34 nm were obtained by a calculation based on the set of 97–141 tilt images using an IMOD software package running on Linux (University of Colorado; Kremer et al., 1996). Corrections for the tilt of the specimen and the long wavelength undulations of the membrane were also achieved with IMOD software. 3D rendering (displaying 3D images in different ways) was performed using the Amira DEV software package (Mercury Computer Systems) operating on a Linux system.

Analysis of the 3D reconstructed images of the MSK

In the series of electron tomography sections shown in Fig. 6 (A and B), the existence of three major classes of filaments with regard to the distance from the membrane surface was found in the following way. The first class is the filaments that are highly electron dense in the first ~0–1.7-nm section (because the contrast is reversed in these micrographs, they look more lucent or white) and are continuously seen in the image sections up to the ~6.8–8.5-nm section, which then dim rapidly in the ~8.5–10.2- and ~10.2–11.9-nm sections. To quantitatively evaluate such signal intensity changes within individual filaments, we selected points that are clearly seen in the image of the first ~0–1.7-nm section every 100–250 nm on each filament, measured the signal intensity on each spot (five pixels), and looked for the section where the signal intensity on the spot decreases by >25% from that for the adjacent section closer to the membrane (the signal intensity tends to drop very rapidly around the threshold sections). If the 25% decrease in the signal intensity occurred between the sections of ~6.8–8.5 and ~8.5–10.2 nm or between the sections of ~8.5–10.2 and ~10.2–11.9 nm, these filaments were categorized into the first class (i.e., those closely associated with the cytoplasmic surface of the cell membrane). These filaments are drawn in green in Fig. 6 C (different regions within a single filament might become dim in either of these two sections).

The second class is similar to the first class but can be seen clearly even in the ~10.2–11.9-nm section (and also in the ~11.9–13.6-nm section, which usually looked similar to the ~10.2–11.9-nm section). This may be the result of the actin filaments that are located several nanometers away from the cytoplasmic surface. Because the platinum rotary shadowing was performed at a low angle (22° from the surface), the platinum may have been deposited in the space between the filament and the membrane. Another possibility is that two filaments are stacked together for a long distance, but we do not think that this happens very often. Therefore, we categorized these filaments into those that stay near the membrane but do not closely associate with the membrane surface. These filaments were not considered to contribute to delimiting the membrane compartments for molecular diffusion in the plasma membrane.

The third class is the filaments that exhibit dim signals in the first ~0–1.7-nm section and show higher electron densities in farther sections, at least up to the section of ~10.2–11.9 nm, before fading out in the ~11.9–13.6- and ~13.6–15.3-nm sections (the latter two sections are not depicted).

These filaments were again assumed not to contribute to forming membrane corrals. The second and third classes of filaments are drawn in red in Fig. 6 C.

There were regions that were not amenable to such analysis. They were the areas where bundles of actin filaments were present (e.g., the structure crossing diagonally from the bottom left to the top right in Fig. 5), actin filaments were too crowded to be individually discerned, an actin filament was terminated in the middle of a domain (domains that contain a loose end of an actin filament), or CCPs, caveolae, and the smooth surface membrane invaginations were present. They were excluded from this analysis (Fig. 7 C, white regions).

Online supplemental material

Video 1 shows a series of 131 tilt images of the undercoat structure on the cytoplasmic surface. Video 2 presents a 3D reconstructed image of the undercoat structure on the cytoplasmic surface of the plasma membrane, which is shown by rotating the reconstructed image. Video 3 shows a series of 97 tilt images of the MSK in an NRK cell, and Video 4 shows a series of 121 sliced images of every 0.85 nm of the MSK of an NRK cell calculated from the data shown in Video 3. Online supplemental material is available at http://www.jcb.org/cgi/content/full/jcb.200606007/DC1.

We thank Y. Hirata (FEI) for her help in starting us with electron tomography, Drs. T. Baba and S. Ohno (Yamanashi University Medical School) for their help in preparing large platinum replicas, Dr. Mitsutoshi Setou (Mitsubishi Kagaku Institute of Life Sciences) for encouragement, and Dr. J. Heuser (Washington University) for helpful discussions and encouragement.

This research was supported, in part, by a Health Labor Sciences Research grant (nano-001 to N. Morone), a National Institute of Biomedical Innovation grant (05-32 to S. Yuasa), and Grants-in-Aid for Scientific Research and on Priority Areas from the Ministry of Education, Culture, Sports, Science and Technology (to J. Usukura and A. Kusumi).

Submitted: 2 June 2006
Accepted: 4 August 2006

References

Apgar, J.R., and M.F. Mescher. 1986. Agorins: major structural proteins of the plasma membrane skeleton of P815 tumor cells. *J. Cell Biol.* 103:351–360.

Bennett, V. 1990. Spectrin-based membrane skeleton: a multipotential adaptor between plasma membrane and cytoplasm. *Physiol. Rev.* 70:1029–1065.

Bennett, V., and L. Chen. 2001. Ankyrins and cellular targeting of divers membrane proteins to physiological sites. *Curr. Opin. Cell Biol.* 13:61–67.

Branton, D., C.M. Cohen, and J. Tyler. 1981. Interaction of cytoskeletal proteins on the human erythrocyte membrane. *Cell.* 24:24–32.

Bussell, S.J., D.A. Hammer, and D.L. Koch. 1994. The effect of hydrodynamic interactions on the tracer and gradient diffusion of integral membrane-proteins in lipid bilayers. *J. Fluid Mech.* 258:167–190.

Bussell, S.J., D.L. Koch, and D.A. Hammer. 1995. Effect of hydrodynamic interactions on the diffusion of integral membrane proteins: diffusion in plasma membranes. *Biophys. J.* 68:1836–1849.

Byers, H.R., and K.R. Porter. 1977. Transformations in the structure of the cytoplasmic ground substance in erythrophores during pigment aggregation and dispersion. I. A study using whole-cell preparations in stereo high voltage electron microscopy. *J. Cell Biol.* 75:541–558.

Discher, D.E., R. Winardi, P.O. Schischmanoff, M. Parra, J.G. Conboy, and N. Mohandas. 1995. Mechanochemistry of protein 4.1's spectrin-actin-binding domain: ternary complex interactions, membrane binding, network integration, structural strengthening. *J. Cell Biol.* 130:897–907.

Edidin, M., S.C. Kuo, and M.P. Sheetz. 1991. Lateral movements of membrane glycoproteins restricted by dynamic cytoplasmic barriers. *Science.* 254:1379–1382.

Fujimoto, K. 1995. Freeze-fracture replica electron microscopy combined with SDS digestion for cytochemical labeling of integral membrane proteins. Application to the immunogold labeling of intercellular junctional complexes. *J. Cell Sci.* 108:3443–3449.

Fujimoto, K., M. Umeda, and T. Fujimoto. 1996. Transmembrane phospholipid distribution revealed by freeze-fracture replica labeling. *J. Cell Sci.* 109:2453–2460.

Fujimoto, L.M., R. Roth, J.E. Heuser, and S.L. Schmid. 2000. Actin assembly plays a variable, but not obligatory role in receptor-mediated endocytosis in mammalian cells. *Traffic.* 1:161–171.

Fujiwara, T., K. Ritchie, H. Murakoshi, K. Jacobson, and A. Kusumi. 2002. Phospholipids undergo hop diffusion in compartmentalized cell membrane. *J. Cell Biol.* 157:1071–1081.

Gaidarov, I., F. Santini, R.A. Warren, and J.H. Keen. 1999. Spatial control of coated-pit dynamics in living cells. *Nat. Cell Biol.* 1:1–7.

Hartwig, J.H., and H.L. Yin. 1988. The organization and regulation of the macrophage actin skeleton. *Cell Motil. Cytoskeleton.* 10:117–125.

Hartwig, J.H., and M. DeSisto. 1991. The cytoskeleton of the resting human blood platelet: structure of the membrane skeleton and its attachment to actin filaments. *J. Cell Biol.* 112:407–425.

Hartwig, J.H., K.A. Chambers, and T.P. Stossel. 1989. Association of gelsolin with actin filaments and cell membranes of macrophages and platelets. *J. Cell Biol.* 108:467–479.

Heuser, J.E. 1983. Procedure for freeze-drying molecules adsorbed to mica flakes. *J. Mol. Biol.* 169:155–195.

Heuser, J.E., and M.W. Kirschner. 1980. Filament organization revealed in platinum replicas of freeze-dried cytoskeletons. *J. Cell Biol.* 86:212–234.

Heuser, J.E., and R.G. Anderson. 1989. Hypertonic media inhibit receptor-mediated endocytosis by blocking clathrin-coated pit formation. *J. Cell Biol.* 108:389–400.

Hirokawa, N., and J.E. Heuser. 1981. Quick-freeze, deep-etch visualization of the cytoskeleton beneath surface differentiations of intestinal epithelial cells. *J. Cell Biol.* 91:399–409.

Iino, R., I. Koyama, and A. Kusumi. 2001. Single molecule imaging of green fluorescent proteins in living cells: E-cadherin forms oligomers on the free cell surface. *Biophys. J.* 80:2667–2677.

Jacobson, K., E.D. Sheets, and R. Simson. 1995. Revisiting the fluid mosaic model of membranes. *Science.* 268:1441–1442.

Katayama, E. 1998. Quick-freeze deep-etch electron microscopy of the actin-heavy meromyosin complex during the in vitro motility assay. *J. Mol. Biol.* 278:349–367.

Kinoshita, M., C.M. Field, M.L. Coughlin, A.F. Straight, and T.J. Mitchison. 2002. Self- and actin-templated assembly of Mammalian septins. *Dev. Cell.* 3:791–802.

Kremer, J.R., D.N. Mastronarde, and J.R. McIntosh. 1996. Computer visualization of three-dimensional image data using IMOD. *J. Struct. Biol.* 116:71–76.

Kusumi, A., and Y. Sako. 1996. Cell surface organization by the membrane skeleton. *Curr. Opin. Cell Biol.* 8:566–574.

Kusumi, A., C. Nakada, K. Ritchie, K. Murase, K. Suzuki, H. Murakoshi, R.S. Kasai, J. Kondo, and T. Fujiwara. 2005. Paradigm shift of the plasma membrane concept from the two-dimensional continuum fluid to the partitioned fluid: high-speed single-molecule tracking of membrane molecules. *Annu. Rev. Biophys. Biomol. Struct.* 34:351–378.

Lucic, V., F. Forster, and W. Baumeister. 2005. Structural studies by electron tomography: from cells to molecules. *Annu. Rev. Biochem.* 74:833–865.

Luna, E.J., and A.L. Hitt. 1992. Cytoskeleton–plasma membrane interactions. *Science.* 258:955–964.

McIntosh, R., D. Nicastro, and D. Mastronarde. 2005. New views of cells in 3D: an introduction to electron tomography. *Trends Cell Biol.* 15:43–51.

Medalia, O., I. Weber, A.S. Frangakis, D. Nicastro, G. Gerisch, and W. Baumeister. 2002. Macromolecular architecture in eukaryotic cells visualized by cryoelectron tomography. *Science.* 298:1209–1213.

Merrifield, C.J., M.E. Feldman, L. Wan, and W. Almers. 2002. Imaging actin and dynamin recruitment during invagination of single clathrin-coated pits. *Nat. Cell Biol.* 4:691–698.

Mohandas, N., and E. Evans. 1994. Mechanical properties of the red cell membrane in relation to molecular structure and genetic defects. *Annu. Rev. Biophys. Biomol. Struct.* 23:787–818.

Moritz, M., M.B. Braunfeld, V. Guenebaut, J. Heuser, and D.A. Agard. 2000. Structure of the gamma-tubulin ring complex: a template for microtubule nucleation. *Nat. Cell Biol.* 2:365–370.

Murase, K., T. Fujiwara, Y. Umemura, K. Suzuki, R. Iino, H. Yamashita, M. Saito, H. Murakoshi, K. Ritchie, and A. Kusumi. 2004. Ultrafine membrane compartments for molecular diffusion as revealed by single molecule techniques. *Biophys. J.* 86:4075–4093.

Pan, Z., T. Kao, Z. Horvath, J. Lemos, J.Y. Sul, S.D. Cranstoun, V. Bennett, S.S. Scherer, and E.C. Cooper. 2006. A common ankyrin-G-based mechanism retains KCNQ and NaV channels at electrically active domains of the axon. *J. Neurosci.* 26:599–613.

Parton, R.G. 2003. Caveolae–from ultrastructure to molecular mechanisms. *Nat. Rev. Mol. Cell Biol.* 4:162–167.

Perkins, G.A., C.W. Renken, J.Y. Song, T.G. Frey, S.J. Young, S. Lamont, M.E. Martone, S. Lindsey, and M.H. Ellisman. 1997. Electron tomography of large, multicomponent biological structures. *J. Struct. Biol.* 120:219–227.

Pollard, T.D., and J.A. Cooper. 1986. Actin and actin-binding proteins. A critical evaluation of mechanisms and functions. *Annu. Rev. Biochem.* 55:987–1035.

Qualmann, B., M.M. Kessels, and R.B. Kelly. 2000. Molecular links between endocytosis and the actin cytoskeleton. *J. Cell Biol.* 150:F111–F116.

Rothberg, K.G., J.E. Heuser, W.C. Donzell, Y.S. Ying, J.R. Glenney, and R.G. Anderson. 1992. Caveolin, a protein component of caveolae membrane coats. *Cell.* 68:673–682.

Rutter, G., W. Bohn, H. Hohenberg, and K. Mannweiler. 1988. Demonstration of antigens at both sides of plasma membranes in one coincident electron microscopic image: a double-immunogold replica study of virus-infected cells. *J. Histochem. Cytochem.* 36:1015–1021.

Sako, Y., and A. Kusumi. 1994. Compartmentalized structure of the plasma membrane for receptor movements as revealed by a nanometer-level motion analysis. *J. Cell Biol.* 125:1251–1264.

Sako, Y., and A. Kusumi. 1995. Barriers for lateral diffusion of transferrin receptor in the plasma membrane as characterized by receptor dragging by laser tweezers: fence versus tether. *J. Cell Biol.* 129:1559–1574.

Sako, Y., A. Nagafuchi, S. Tsukita, M. Takeichi, and A. Kusumi. 1998. Cytoplasmic regulation of the movement of E-cadherin on the free cell surface as studied by optical tweezers and single particle tracking: corralling and tethering by the membrane skeleton. *J. Cell Biol.* 140:1227–1240.

Sanan, D.A., and R.G. Anderson. 1991. Simultaneous visualization of LDL receptor distribution and clathrin lattices on membranes torn from the upper surface of cultured cells. *J. Histochem. Cytochem.* 39:1017–1024.

Saxton, M.J. 1989. The spectrin network as a barrier to lateral diffusion in erythrocytes. A percolation analysis. *Biophys. J.* 55:21–28.

Saxton, M.J. 1990. The membrane skeleton of erythrocytes. A percolation model. *Biophys. J.* 57:1167–1177.

Saxton, M.J., and K. Jacobson. 1997. Single-particle tracking: applications to membrane dynamics. *Annu. Rev. Biophys. Biomol. Struct.* 26:373–399.

Schoenenberger, C.A., M.O. Steinmetz, D. Stoffler, A. Mandinova, and U. Aebi. 1999. Structure, assembly, and dynamics of actin filaments in situ and in vitro. *Microsc. Res. Tech.* 47:38–50.

Sheetz, M.P. 1983. Membrane skeletal dynamics: role in modulation of red cell deformability, mobility of transmembrane proteins, and shape. *Semin. Hematol.* 20:175–188.

Sheetz, M.P., and D. Sawyer. 1978. Triton shells of intact erythrocytes. *J. Supramol. Struct.* 8:399–412.

Sheetz, M.P., J.E. Sable, and H.G. Dobereiner. 2006. Continuous membrane-cytoskeleton adhesion requires continuous accommodation to lipid and cytoskeleton dynamics. *Annu. Rev. Biophys. Biomol. Struct.* 35:417–434.

Shen, B.W., R. Josephs, and T.L. Steck. 1986. Ultrastructure of the intact skeleton of the human erythrocyte membrane. *J. Cell Biol.* 102:997–1006.

Suzuki, K., K. Ritchie, E. Kajikawa, T. Fujiwara, and A. Kusumi. 2005. Rapid hop diffusion of a G-protein-coupled receptor in the plasma membrane as revealed by single-molecule techniques. *Biophys. J.* 88:3659–3680.

Takeuchi, M., H. Miyamoto, Y. Sako, H. Komizu, and A. Kusumi. 1998. Structure of the erythrocyte membrane skeleton as observed by atomic force microscopy. *Biophys. J.* 74:2171–2183.

Tomishige, M., Y. Sako, and A. Kusumi. 1998. Regulation mechanism of the lateral diffusion of band 3 in erythrocyte membranes by the membrane skeleton. *J. Cell Biol.* 142:989–1000.

Tsuji, A., and S. Ohnishi. 1986. Restriction of the lateral motion of band 3 in the erythrocyte membrane by the cytoskeletal network: dependence on spectrin association state. *Biochemistry.* 25:6133–6139.

Tsuji, A., K. Kawasaki, S. Ohnishi, H. Merkle, and A. Kusumi. 1988. Regulation of band 3 mobilities in erythrocyte ghost membranes by protein association and cytoskeletal meshwork. *Biochemistry.* 27:7447–7452.

Tsukita, S., S. Tsukita, and H. Ishikawa. 1980. Cytoskeletal network underlying the human erythrocyte membrane. Thin-section electron microscopy. *J. Cell Biol.* 85:567–576.

Tsukita, S., S. Yonemura, and S. Tsukita. 1997. ERM proteins: head-to-tail regulation of actin-plasma membrane interaction. *Trends Biochem. Sci.* 22:53–58.

Ursitti, J.A., D.W. Pumplin, J.B. Wade, and R.J. Bloch. 1991. Ultrastructure of the human erythrocyte cytoskeleton and its attachment to the membrane. *Cell Motil. Cytoskeleton.* 19:227–243.

Usukura, J., and E. Yamada. 1987. Ultrastructure of the synaptic ribbons in photoreceptor cells of *Rana catesbeiana* revealed by freeze-etching and freeze-substitution. *Cell Tissue Res.* 247:483–488.

Valentijn, J.A., K. Valentijn, L.M. Pastore, and J.D. Jamieson. 2000. Actin coating of secretory granules during regulated exocytosis correlates with the release of rab3D. *Proc. Natl. Acad. Sci. USA.* 97:1091–1095.

Wuestehube, L.J., and E.J. Luna. 1987. F-actin binds to the cytoplasmic surface of ponticulin, a 17-kD integral glycoprotein from *Dictyostelium discoideum* plasma membranes. *J. Cell Biol.* 105:1741–1751.

Zeuschner, D., W.J. Geerts, E. van Donselaar, B.M. Humbel, J.W. Slot, A.J. Koster, and J. Klumperman. 2006. Immuno-electron tomography of ER exit sites reveals the existence of free COPII-coated transport carriers. *Nat. Cell Biol.* 8:377–383.

Glycobiology vol. 16 no. 8 pp. 702–710, 2006
doi:10.1093/glycob/cwj115
Advance Access publication on April 19, 2006

N-Acetylglucosamine 6-*O*-sulfotransferase-1 is required for brain keratan sulfate biosynthesis and glial scar formation after brain injury

Haoqian Zhang[2], Takashi Muramatsu[1,3], Atsushi Murase[2], Shigeki Yuasa[4], Kenji Uchimura[5], and Kenji Kadomatsu[1,2,6]

[2]Department of Biochemistry, Nagoya University Graduate School of Medicine, Nagoya 466-8550, Japan; [3]Department of Health Science, Faculty of Psychological and Physical Sciences, Aichi Gakuin University, Aichi 470-0195, Japan; [4]Department of Ultrastructural Research, National Institute of Neuroscience, National Center of Neurology and Psychiatry, Kodaira, Tokyo 187-8502, Japan; [5]Department of Anatomy, Program in Immunology, University of California, San Francisco, CA 94143; and [6]Institute for Advanced Research, Nagoya University, Furo-cho, Chikusa-ku, Nagoya 464-8601, Japan

Received on December 17, 2005; revised on March 28, 2006; accepted on April 10, 2006

Keratan sulfate (KS) is a glycosaminoglycan composed of repeating disaccharide units with sulfate residues at the C6 positions of galactose and *N*-acetylglucosamine (GlcNAc). The *N*-acetylglucosamine 6-*O*-sulfotransferase(s) (GlcNAc6ST) involved in the synthesis of KS in the central nervous system (CNS) has long been unidentified. Here, we report that a deficiency of GlcNAc6ST-1 leads to loss of 5D4-reactive brain KS and reduction of glial scar formation after cortical stab injury in mice. During the development of mice deficient in GlcNAc6ST-1, KS expression in the brain was barely detectable with the KS-specific antibody 5D4. The reactivity of 5D4 antibody with protein tyrosine phosphatase ζ (PTPζ), a KS proteoglycan (KSPG), was abolished in the deficient mice. In adults, brain injury induced 5D4-reactive KS synthesis in the wounded area in wild-type (WT) mice but not in the deficient mice. Glial scar is formed via the accumulation of reactive astrocytes and is a major obstacle to axonal regeneration by injured neurons. Reactive astrocytes appeared to similar extents in the two genotypes, but they accumulated in the wounded area to a lesser extent in the deficient mice. Consequently, the deficient mice exhibited a marked reduction of scarring and enhanced neuronal regeneration after brain injury. These findings highlight the indispensable role of GlcNAc6ST-1 in brain KS biosynthesis and glial scar formation after brain injury.

Key words: axon regeneration/glial scar/keratan sulfate/*N*-acetylglucosamine 6-*O*-sulfotransferase/reactive astrocytes

Introduction

Keratan sulfate (KS) is a glycosaminoglycan, which is formed through the elongation of *N*- or *O*-glycans covalently attached to scaffold proteins. KS-bearing proteins are known as KS proteoglycans (KSPGs) and are found in the extracellular matrix and on the cell surface (Kleene and Schachner, 2004). KS is composed of repeating disaccharide units of galactose and *N*-acetylglucosamine (GlcNAc), with sulfate groups at the C6 positions of galactose and GlcNAc. The sulfation modification of GlcNAc residues is mediated by GlcNAc-6-*O*-sulfotransferase (GlcNAc6ST) (Fukuda *et al.*, 2001). Human corneal GlcNAc6ST (C-GlcNAc6ST/GlcNAc6ST-5/CHST6) is critical for KS synthesis in the cornea (Akama *et al.*, 2000, 2001), which is a tissue that contains abundant KSPGs (Nilsson *et al.*, 1983). A previous study showed that sulfation on the C6 positions of GlcNAc residues is necessary for KS chain elongation (Akama *et al.*, 2001).

KS is also expressed in central nervous tissues (Miller *et al.*, 1997). Interestingly, KS synthesis is up-regulated in the lesions on central nervous system (CNS) injury (Jones and Tuszynski, 2002). The adult mammalian CNS does not spontaneously regenerate after injury. The failure of the regeneration of injured axons is widely acknowledged to be due to a combination of factors, including the emergence of a molecular barrier because of the up-regulation of growth-inhibiting molecules such as inhibitors within myelin and chondroitin sulfate proteoglycans (CSPGs), and the formation of a physical barrier by reactive astrocytes ("glial scar") (Horner and Gage, 2000; Filbin, 2003; McGee and Strittmatter, 2003; Schnaar, 2003; Silver and Miller, 2004). However, molecular mechanisms underlying the glial scar formation have not been well understood.

GlcNAc6ST-1 mRNA is expressed in various tissues including the brain (Uchimura *et al.*, 1998; Fan *et al.*, 1999). Here, we demonstrate that KS, which is recognized by the KS-specific antibody 5D4, is abrogated in the brains of GlcNAc6ST-1-deficient (GlcNAc6ST-1$^{-/-}$) mice. Moreover, taking advantage of that condition of the deficient mice, we found that KS plays an indispensable role in glial scar formation after brain injury.

Results

Loss of 5D4 and EFG11 reactivity in GlcNAc6ST-1$^{-/-}$ mice during development

We first examined KS expression in the developing brain, because we had found that GlcNAc6ST-1 mRNA is expressed in the thalamus of mouse embryos (Fan *et al.*, 1999). The 5D4 antibody specifically recognizes KS (Scudder *et al.*, 1986). 5D4-reactive KS expression was detected in the embryonic thalamus and cerebral cortex in wild-type (WT) mice but not in GlcNAc6ST-1$^{-/-}$ mice (Figure 1A and B). By contrast, 5D4-reactive KS was expressed in the cartilage of developing vertebrae in a similar manner in the

[1]To whom correspondence should be addressed; e-mail: tmurama@dpc.aichi-gakuin.ac.jp/kkadoma@med.nagoya-u.ac.jp

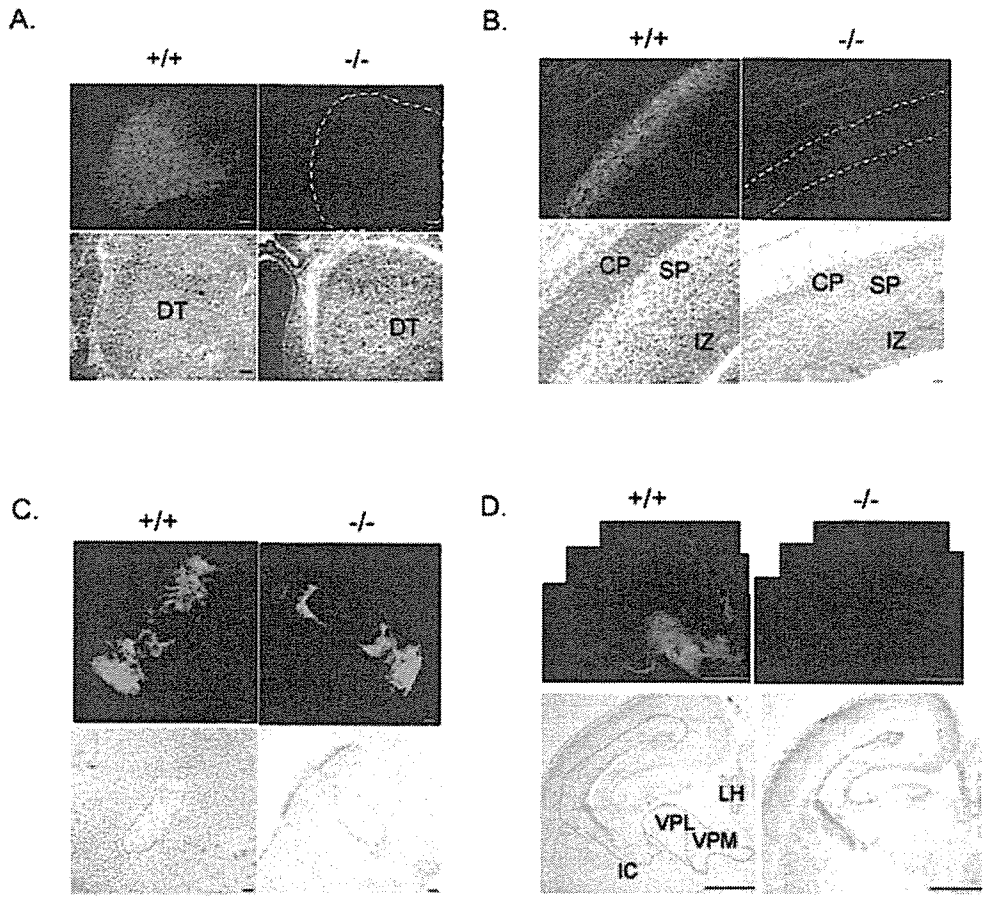

Fig. 1. 5D4-positive signals are absent in the brain, but not the vertebrae, in GlcNAc6ST-1$^{-/-}$ mice during development. **(A)** Brain specimens obtained from embryonic day 15.5 mice were stained with 5D4 antibody. The results for WT (+/+) and GlcNAc6ST-1$^{-/-}$ (-/-) mice are shown. Dark field photos show KS expression in red color. Bright field photos show hematoxylin staining. DT, dorsal thalamus. Bars: 250 μm. **(B)** Brain specimens obtained from embryonic day 15.5 mice were stained with 5D4 antibody. Dark field photos show KS expression in red color. Bright field photos show hematoxylin staining. CP, cortical plate; DT, dorsal thalamus; IZ, intermediate zone; SP, subplate. **(C)** Vertebra specimens from embryonic day 15.5 mice were stained with 5D4 antibody. Bright field photos show hematoxylin and eosin staining. **(D)** Brain specimens on postnatal day 1 were also stained with 5D4 antibody. Bright field photos show hematoxylin and eosin staining. IC, internal capsule; LH, lateral hypothalamic area; VPL, ventral posterolateral thalamic nucleus; VPM, ventral posteromedial thalamic nucleus. Bars: 250 μm.

two genotypes (Figure 1C). On postnatal day 1, 5D4-reactive KS was expressed in several nuclei in the thalamus and the projecting route from the thalamus to the cortex in WT mice, this being consistent with a previous report describing 5D4-reactive KS expression in rat brain (Miller *et al.*, 1997) (Figure 1D). This expression had completely disappeared in GlcNAc6ST-1$^{-/-}$ mice (Figure 1D).

KS expression in WT mouse brain was further confirmed by means of western blot analysis with 5D4. Broad bands corresponding to between 250 and 150 kDa, and higher than 250 kDa, appeared on postnatal days 1 and 8 and had diminished slightly on day 15 (Figure 2A). A band higher than 250 kDa is indicated by asterisks shown in Figure 2E. Digestion of WT brain samples with keratanase I or keratanase II significantly decreased the 5D4 reactivity observed on western blot, indicating the specificity of this antibody (Figure 2B). Both 5D4 and EFG11, which recognizes poorly sulfated KS, detected the smear bands for WT mice brain but not for GlcNAc6ST-1$^{-/-}$ mice (Figure 2C and D).

Protein tyrosine phosphatase ζ (PTPζ)/phosphacan is known to be a KS-bearing proteoglycan in the nervous system (Maeda *et al.*, 1995). The 6B4 antibody recognizes this proteoglycan and precipitated similar amounts of PTPζ in the two genotypes (Figure 2E, left). However, only the precipitate obtained with 6B4 antibody from WT mice, that is, not that from GlcNAc6ST-1$^{-/-}$mice, contained 5D4-reactive KS (Figure 2E, left). Similarly, the 5D4 antibody only precipitated PTPζ in WT mice (Figure 2E, right). These data collectively indicate that the loss of GlcNAc6ST-1 leads to the abrogation of 5D4-reactive KS in the embryonic and neonatal brains of mice.

Loss of 5D4-staining signals in GlcNAc6ST-1$^{-/-}$ mice after brain injury

Despite such a specific expression profile of KS during development, GlcNAc6ST-1$^{-/-}$ mice did not show any apparent abnormalities of the CNS. It is known that KS

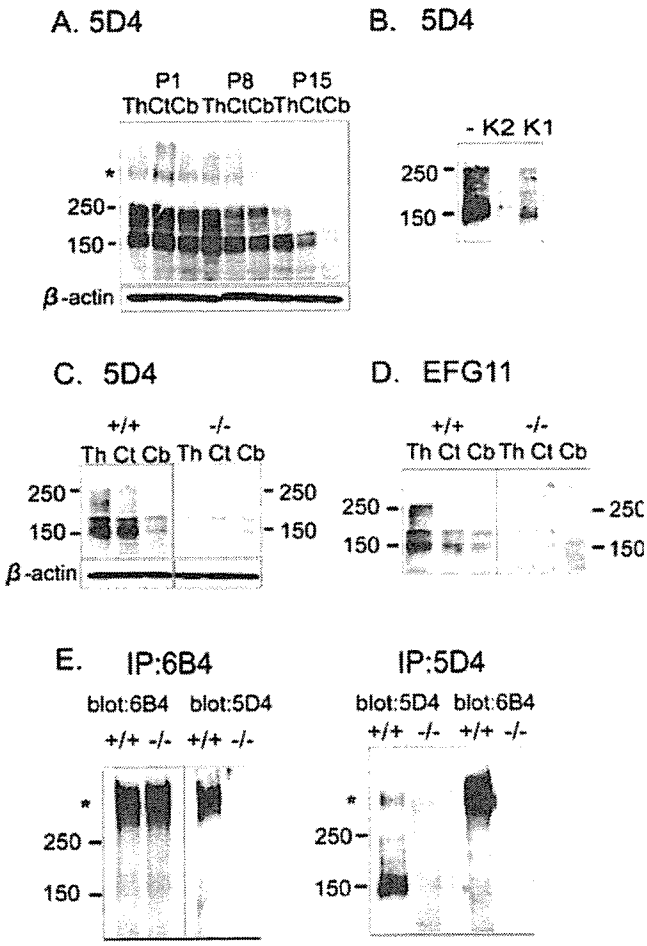

Fig. 2. Western blot analysis of KSPGs. (**A**) Samples were extracted from the thalamus (Th), cerebral cortex (Ct), and cerebellum (Cb) of WT mice on postnatal days 1, 8, and 15. The western blot was probed with 5D4 antibody. The blot was also probed with anti-β actin antibody to show the equal loading of protein samples. The asterisk indicates a band higher than 250 kDa and corresponds to asterisks appearing in (**E**). (**B**) Samples from the brains of postnatal day 8 WT mice were digested with keratanase I (K1) or keratanase II (K2) and then subjected to western blot analysis with 5D4 antibody. (**C**) Brain samples obtained from WT and GlcNAc6ST-1$^{-/-}$ mice on postnatal day 8 were subjected to western blot with 5D4 antibody. The blot was probed with anti-β actin antibody to show the equal loading of protein samples. (**D**) Western blot was performed with EFG11 antibody for the samples used in (**C**). (**E**) Left panel: samples from postnatal 8-day mouse thalamus after treating with chondroitinase ABC were precipitated with anti-PTPζ antibody 6B4 and then blotted, followed by probing with either 5D4 antibody or 6B4 antibody. Right panel: samples from postnatal 8-day mouse thalamus after treating with chondroitinase ABC were precipitated with 5D4 antibody and then probed with 6B4 antibody or 5D4 antibody. Asterisks correspond to the asterisk in (**A**).

expression is substantially induced by injury in a model of rat spinal cord injury, as revealed by 5D4 antibody immunostaining (Jones and Tuszynski, 2002). To study the biological function of KS in CNS injury, we performed an assay in which a stab wound was made to the cerebral cortex. 5D4-reactive KS expression became apparent in WT mice 4 days after injury, reached the maximum level at 7 days, and then gradually decreased (Figure 3A). However, the induction of

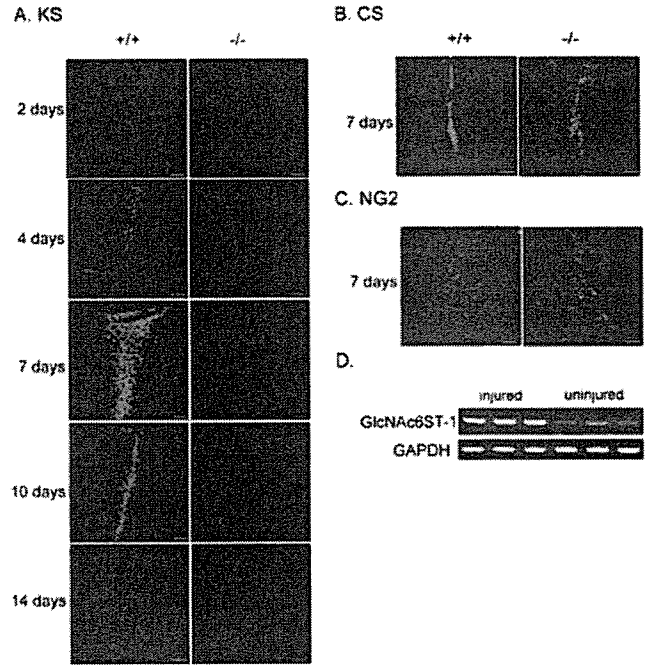

Fig. 3. KS expression is not induced by injury in GlcNAc6ST-1$^{-/-}$ mice. (**A**) KS expression following a stab wound was monitored by means of immunofluorescence staining. Days after a stab wound are indicated on the left of each row. At least three mice were examined for each time point and showed similar results. Representative photos are shown. Bars: 250 μm. (**B, C**) CS (**B**) and NG2 (**C**) expression at 7 days after a stab wound. Data of 7 days after injury in **A**, **B**, and **C** are serial sections from the same mouse. Three mice were examined and showed similar results. Representative photos are shown. Bars: 250 μm. (**D**) Total RNAs from WT mouse cerebral cortices injured with a knife cut (14 days after operation) or normal controls were used to synthesize cDNAs. Fragments corresponding to GlcNAc6ST-1 (491 bp) and GAPDH (500 bp) were amplified by PCR using the cDNAs as templates. Six WT mice (three for injured and three for control samples) were used.

5D4-reactive KS expression was not observed in GlcNAc6ST-1$^{-/-}$ mice (Figure 3A). Chondroitin sulfate (CS) expression was induced to similar extents in the two genotypes (Figure 3B). Consistently, NG2, a CSPG, was induced in both genotypes (Figure 3C) (Jones *et al.*, 2002). Supporting the results of 5D4-reactive KS expression induction in WT mice, GlcNAc6ST-1 expression was strongly up-regulated by injury, as revealed by reverse transcription–polymerase chain reaction (RT–PCR) using knife-cut injury samples (Figure 3D).

Reduction of glial scar formation in GlcNAc6ST-1$^{-/-}$ mice after brain injury

Glial fibrillary acidic protein (GFAP) is a marker for reactive astrocytes. In WT mice, reactive astrocytes appeared around the wounded area 2 days after injury and had accumulated around the lesion by 7 days (Figure 4A). The accumulation was most prominent at 10 days and then gradually decreased (Figure 4A). However, the astrocyte accumulation was strikingly reduced in GlcNAc6ST-1$^{-/-}$ mice, although reactive astrocytes appeared around the wounded area to an extent similar to that in WT mice at

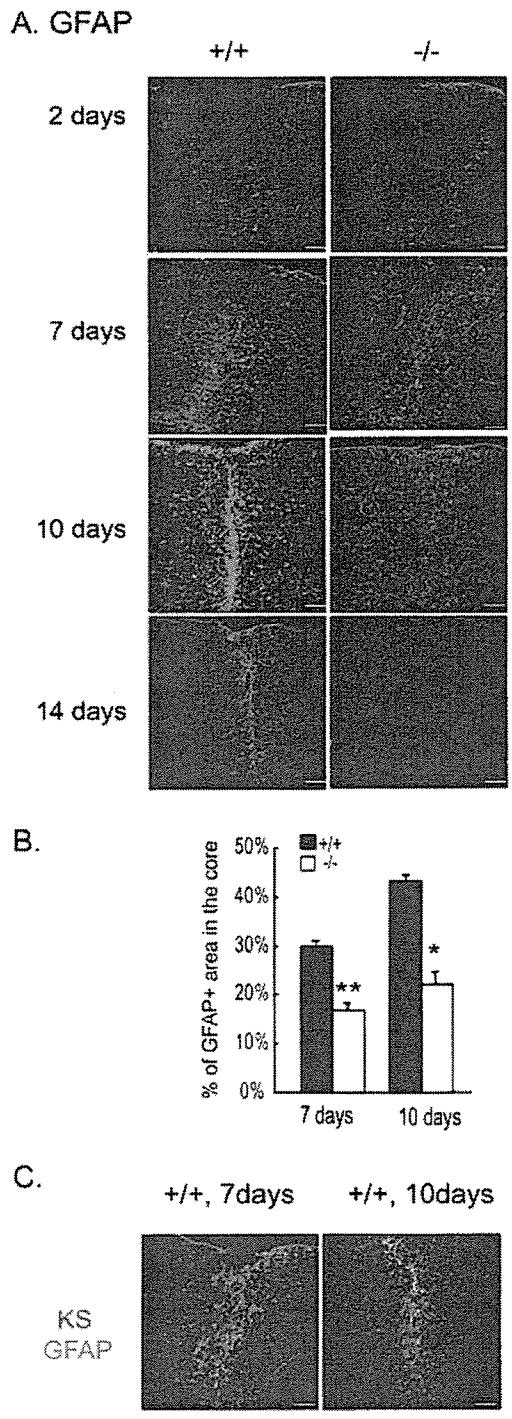

Fig. 4. Reactive astrocyte accumulation following a stab wound is strikingly reduced in GlcNAc6ST-1$^{-/-}$ mice. (**A**) Anti-GFAP antibody was used for this immunofluorescence staining. Days after a stab wound are shown on the left side of each row. At least three mice were examined for each time point and showed similar results. Representative photos are shown. Bars: 250 μm. (**B**) The accumulation of reactive astrocytes at 7 and 10 days after injury is presented as a ratio of GFAP-positive cells in the lesion core versus those in the whole area of obtained images. The quantification method is described in *Materials and Methods*. $^{**}p < 0.001$; $^{*}p < 0.01$. (**C**) Double staining using anti-GFAP and anti-KS 5D4 was performed. Three mice were examined for each time point and showed similar results. Representative photos are shown. Bars: 250 μm.

2 days (Figure 4A). Quantitative analysis revealed that the accumulation of reactive astrocytes around the injured lesion was significantly suppressed in GlcNAc6ST-1$^{-/-}$ mice (Figure 4B, methods are described in *Materials and Methods*). Interestingly, the 5D4-reactive KS expression area was more restricted than the reactive astrocyte accumulation area 7 days after injury in WT mice (Figure 4C). Taking the temporal profiles of 5D4-reactive KS expression (peak at 7 days after injury; Figure 3A) and reactive astrocyte accumulation (peak at 10 days; Figure 4A) into account, the results indicate that reactive astrocytes migrated to the 5D4-reactive KS-expressing area, that is, the lesion core, in WT mice. Figure 4C also demonstrates that cells expressing 5D4-reactive KS and GFAP did not overlap. This is consistent with a previous report that 5D4-reactive KS is produced by invading macrophages, microglia, and oligodendrocyte precursors but not by astrocytes in spinal cord injury (Jones and Tuszynski, 2002).

Collagen IV appears at late stages of glial scarring (Liesi and Kauppila, 2002) and is associated with an activity that inhibits axonal regeneration (Stichel *et al.*, 1999). Collagen IV expression in the wounded area became apparent 14 days after injury in WT mice, whereas it was negligible in the wounded area in GlcNAc6ST-1$^{-/-}$ mice (Figure 5), this being consistent with the very low accumulation of reactive astrocytes in these mice (Figure 4A). These results support the conclusion that glial scarring was markedly reduced in GlcNAc6ST-1$^{-/-}$ mice.

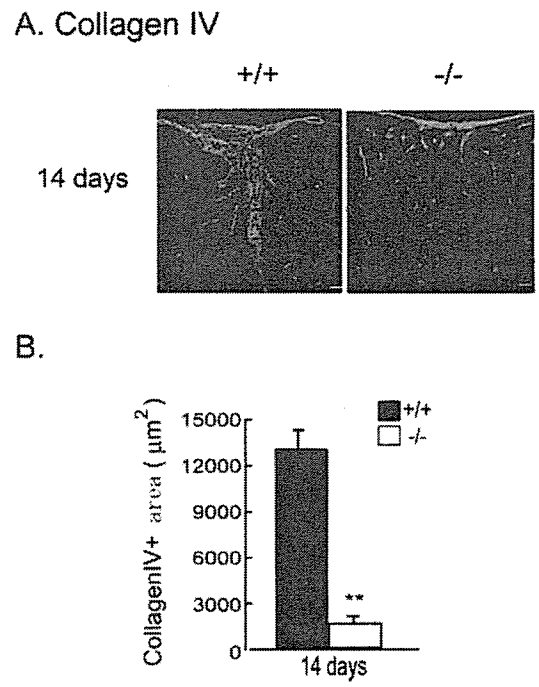

Fig. 5. Collagen IV expression following a stab wound is strikingly reduced in GlcNAc6ST-1$^{-/-}$ mice. (**A**) Collagen IV staining of brain samples at 14 days after injury. Three mice were examined and showed similar results. Representative photos are shown. Bars: 250 μm. (**B**) Quantification of the collagen IV-positive area at 14 days after injury was performed as described in *Materials and Methods*. $^{**}p < 0.001$.

Enhancement of axonal regeneration in GlcNAc6ST-1$^{-/-}$ mice after brain injury

Coinciding with the abolished 5D4-reactive KS expression and poor glial scar formation, axonal regeneration was pronounced in GlcNAc6ST-1$^{-/-}$ mice. The SMI312 antibody can detect phosphoneurofilaments, particularly those of regenerating axons of injured neurons (King *et al.*, 2001). SMI312-positive signals were much more conspicuous at 4 and 7 days after injury in GlcNAc6ST-1$^{-/-}$ mice than in WT mice (Figure 6A and B). Another marker for regenerating axons, anti-growth-associated protein-43 (GAP-43) (King *et al.*, 2001; Bradbury *et al.*, 2002), also demonstrated enhanced axonal regeneration in GlcNAc6ST-1$^{-/-}$ mice (Figure 6C).

Discussion

GlcNAc6ST-1, together with GlcNAc6ST-2, has been regarded as an enzyme required for the synthesis of an L-selectin determinant, sialyl 6-sulfo Le^x, on high endothelial venules in lymph nodes (Hemmerich *et al.*, 2001; Uchimura *et al.*, 2004). More recently, we have demonstrated that mice deficient in both GlcNAc6ST-1 and GlcNAc6ST-2 genes exhibit the elimination of sialyl 6-sulfo Le^x on high endothelial venules and striking reduction of lymphocyte homing (Kawashima *et al.*, 2005; Uchimura *et al.*, 2005). In contrast, the GlcNAc6ST(s) involved in the synthesis of KS in CNS has long been unidentified. Our previous studies showed that GlcNAc6ST-1 transcripts are expressed in the neocortex and dorsal thalamus of mouse embryos (Fan *et al.*, 1999). These results strongly support that the loss of 5D4-reactive KS in the brain, including the neocortex and dorsal thalamus, of GlcNAc6ST-1$^{-/-}$ mouse embryos is attributable to deficiency of C-6 sulfation of GlcNAc residues in KS mediated by GlcNAc6ST-1. The up-regulation of GlcNAc6ST-1 mRNA in the injured brains of adult mice revealed by RT–PCR correlates with highly induced synthesis of 5D4-reactive KS in the lesions on injury in WT mice. This induction was not seen in GlcNAc6ST-1$^{-/-}$ mice after injury, indicating that GlcNAc6ST-1 is the enzyme that elaborates 5D4-reactive KS in the injured brains of adult mice. This is the first evidence that GlcNAc6ST-1 is an enzyme that is involved in GlcNAc-6-sulfation of KS in the mouse CNS. GlcNAc is also one of the disaccharides that make up heparan sulfate and hyaluronic acid. We previously showed that GlcNAc6ST-1 does not exhibit any activity toward completely desulfated *N*-resulfated heparin (Uchimura *et al.*, 1998). In addition, the existence of sulfated hyaluronic acid has not been reported so far. Thus, we conclude that the loss of GlcNAc6ST-1 only affects the synthesis of KS among glycosaminoglycans.

To address a possible role of poly-*N*-acetyllactosamine in the recovery after brain injury, we performed a lectin blot analysis using *Erythrina cristagalli* lectin (ECA). ECA recognizes *N*-acetyllactosamine and poly-*N*-acetyllactosamine, the latter signal becoming faint after endo-β-galactosidase digestion. We found that ECA-reactive signals became stronger after brain injury to similar extents in the two genotypes, that is, WT and GlcNAc6ST-1$^{-/-}$ mice (data not shown). However, those signals were only slightly weaker after endo-β-galactosidase digestion (data not shown). Therefore, it is not likely that poly-*N*-acetyllactosamine plays a major role in the recovery after brain injury in

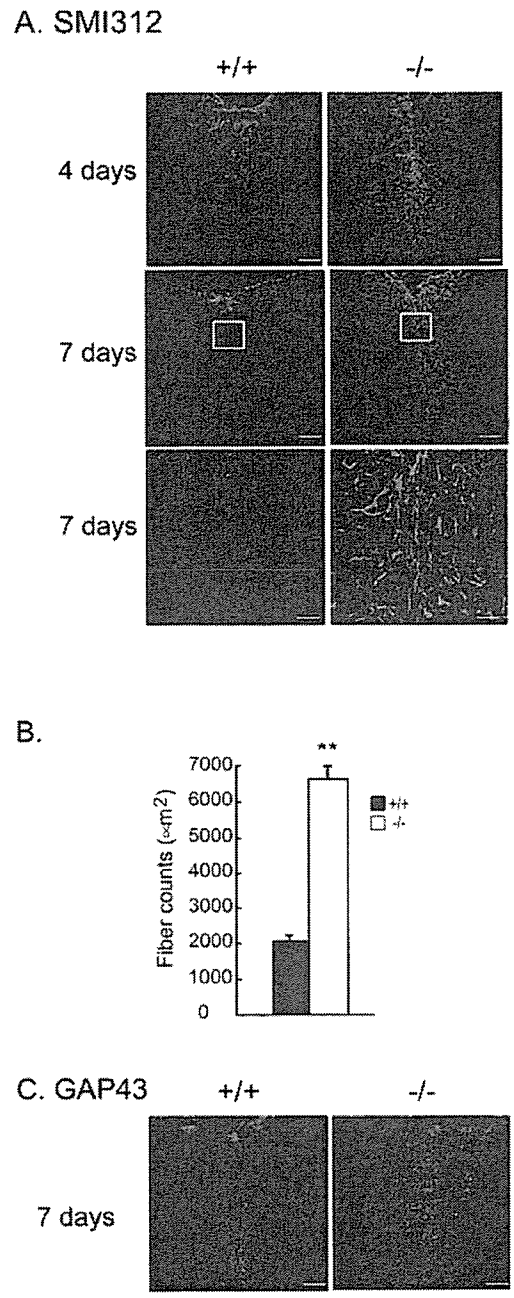

Fig. 6. Neuronal regeneration is enhanced in GlcNAc6ST-1$^{-/-}$ mice. To monitor neuronal regeneration, SMI132 (**A**) and GAP-43 (**C**) antibodies were used. SMI132-positive fibers at 7 days after injury (**B**) was also quantified as described in *Materials and Methods*. The photos in the second row in (**A**) are higher magnifications of areas (squares) depicted than those in the first row. Data of 7 days after injury in (**A**) and (**C**) are serial sections from the same mouse. Days after a stab wound are shown on the left side of each row. At least three mice were examined for each time point and showed similar results. Representative photos are shown. Bars represent 250 μm, except for the second row in (**A**), in which bars represent 62.5 μm. $^{**}p < 0.001$.

GlcNAc6ST-1$^{-/-}$ mice. This idea is supported by literatures, showing that synthesis of KS is independent of that of poly-*N*-acetyllactosamine (Akama *et al.*, 1998, 2001; Lee *et al.*, 2000; Uchimura *et al.*, 2002; Seko *et al.*, 2003; Seko and Yamashita, 2004). Thus, in the KS repeating units of Galβ1-4GlcNAcβ1-3, GlcNAc is always 6-sulfated and Gal is occasionally sulfated. The sequence of KS biosynthesis is *N*-acetylglucosaminylation, 6-sulfation of a GlcNAc residue exposed at the non-reducing end, and galactosylation.

A stab wound induced the appearance of reactive astrocytes in GlcNAc6ST-1$^{-/-}$ mice, which was comparable with that in WT mice. Surprisingly, however, reactive astrocyte accumulation in the lesion core and subsequent collagen IV expression were markedly reduced in GlcNAc6ST-1$^{-/-}$ mice. These *in vivo* results suggest that 5D4-reactive KS itself or attractive factors recruited to 5D4-reactive KS in the lesion core may promote astrocyte accumulation. Although the mechanism of KS-mediated astrocyte migration remains to be verified, our data highlight an indispensable function of KS in the migration of reactive astrocytes and glial scar formation.

KSPGs are expressed in the roof plate of the developing spinal cord, being involved in barrier formation during ontogenesis (Snow *et al.*, 1990; Cole and McCabe, 1991). Moreover, treatment with keratanase but not with chondroitinase ABC leads to enhanced outgrowth and the regeneration of transected mossy fiber in rat hippocampal slice cultures (Butler *et al.*, 2004). These results suggest a non-permissive role of KS as to neuronal regeneration. This is supported by our finding that the enhancement of axonal regeneration started in GlcNAc6ST-1$^{-/-}$ mice at 4 days after injury when 5D4-reactive KS expression was up-regulated in WT mice, this timing being earlier than that of apparent accumulation of astrocytes in WT mice (7 days after injury). It is also known that KS inhibits axonal outgrowth *in vitro* (Dou and Levine, 1995). Therefore, our results further support the importance of KS's inhibitory activity as to axonal growth.

The two roles (as to glial scar formation and neuronal regeneration) of KS addressed above could be more clearly understood by comparing KS with CS. One of the most important findings in the present study is that CS expression was induced to similar extents in both WT and GlcNAc6ST-1$^{-/-}$ mice, although glial scarring was suppressed and neuronal regeneration was enhanced in GlcNAc6ST-1$^{-/-}$ mice. Historically, CSPGs have been paid attention as non-permissive cues for neuronal regeneration (Snow *et al.*, 1990; Davies *et al.*, 1997; McKeon *et al.*, 1999; Properzi *et al.*, 2005). The inhibitory effect of CSPGs on axonal outgrowth is largely ascribed to their covalently attached CS glycosaminoglycans. Thus, an attempt to ablate CS is now a candidate therapeutic for the CNS injury (Moon *et al.*, 2001; Bradbury *et al.*, 2002; Grimpe and Silver, 2004). Besides this non-permissive role, CSPGs also play a central role in the formation of the perineuronal net, which keeps the cell membranes of neurons apart, through binding with hyaluronan and tenascin (Roitbak and Sykova, 1999; Fox and Caterson, 2002; Dityatev and Schachner, 2003). As chondroitinase ABC degrades CS and even hyaluronan, chondroitinase ABC treatment probably destroys the perineuronal net and thereby generates a milieu allowing neurons to interact with one another more freely. In this context, the present results were unpredictable because KS comprises a very small fraction of glycosaminoglycans, as compared with CS, in the brain, and therefore, it was hard to expect that the loss of KS causes extensive disorganization of the perineuronal net. The appearance of the phenotypes (reduced glial scarring and enhanced regeneration) in GlcNAc6ST-1$^{-/-}$ mice suggests that the roles of KS and CS are, at least in part, separately required for biological responses to CNS injury. Thus, CS not only acts as a non-permissive cue but also is involved in the formation of a physical barrier together with accumulated reactive astrocytes through the formation of a firm perineuronal net. On the contrary, KS initiates the formation of a physical barrier by inducing reactive astrocyte accumulation and also acts as a non-permissive cue.

It is noteworthy that anatomical regeneration after chondroitinase ABC treatment is limited, suggesting that other inhibitory factors and/or mechanisms may underlie axonal regeneration in mammals (Bradbury *et al.*, 2002). Our data suggest that ablation of KS or combined ablation of KS and CS could be a candidate therapeutic for CNS injury. An apparent candidate method for KS ablation is keratanase treatment. As currently available keratanase is too labile for *in vivo* use, further improved manufacturing will facilitate keratanase application.

Materials and methods

Mice

GlcNAc6ST-1$^{-/-}$ mice were produced using D3 embryonic stem cells and an ordinary gene targeting technology as previously described (Uchimura *et al.*, 2004). GlcNAc6ST-1$^{+/-}$ mice obtained after backcrossing with C57BL/6J for more than seven generations were interbred, and the littermates obtained were used for the brain injury experiments. These mice were maintained in the animal facilities of Nagoya University. All experiments were performed in accordance with protocols approved by the institutional animal committee.

Reagents

Anti-KS 5D4 antibody and biotin-conjugated one were purchased from Seikagaku (Tokyo, Japan). EFG11 was from Chemicon, USA. Anti-CS CS-56 antibody, Cy3-conjugated anti-GFAP antibody, and fluoresceinisothiocyanate (FITC)-conjugated anti-mouse IgG were from Sigma (Kanagawa, Japan); anti-phosphoneurofilament SMI312 from Sternberger Monoclonals (Lutherville, MD); anti-GAP-43 and anti-NG2 from Chemicon; and anti-type IV collagen from LSL (Tokyo, Japan). Cy3- or Cy2-conjugated streptavidin and Cy3-conjugated anti-mouse IgM were from Jackson ImmunoResearch (West Grove, PA); Cy3-conjugated anti-rabbit IgG from Zymed (Tokyo, Japan); FITC-conjugated anti-rabbit IgG from Cappel (Irvine, CA); and anti-β actin antibody from Sigma. FluorSave was obtained from Calbiochem, (Tokyo, Japan).

Immunohistochemistry

Tissues were cut into 5-μm sections with a cryostat and mounted on glass slides. Sections were fixed with cold acetone

for 5 min, dried, and then blocked in phosphate-buffered saline (PBS) containing 3% bovine serum albumin (BSA) and 5% normal mouse serum for staining of biotin-conjugated anti-KS 5D4 or blocked in PBS containing 1% BSA and 10% normal goat serum for other immunohistochemistry. Sections were then incubated with the primary antibodies at 100× dilution in a blocking solution overnight at 4°C or 1 h at room temperature. After rinsing, they were incubated with the secondary antibody (Cy3- or Cy2-conjugated streptavidin, 1/500; Cy3-conjugated goat anti-rabbit IgG, 1/100; Cy3-conjugated goat anti-mouse IgM, 1/200; or FITC-conjugated goat anti-rabbit IgG, 1/200) for 30 min at room temperature, rinsed, and then mounted with FluorSave and examined by confocal microscopy (MRC 1024; Bio-Rad, Tokyo, Japan).

Immunoblots and immunoprecipitations

The cerebral cortex and thalamus were dissected from the brains of P1, P8, and P15 mouse and homogenized in PBS including 1% Triton X-100 and protease inhibitors solution (Sigma). Samples of the supernatant fraction were collected after centrifuging at 10,000 *g* for 30 min and were separated by electrophoresis on 6% SDS–PAGE. Proteins were then blotted onto nitrocellulose membranes. Blots were blocked with 5% fat-free dry milk in PBS containing 0.3% Triton X-100 for 60 min and incubated overnight at 4°C with the primary antibody anti-KS 5D4 (1 μg/mL) or EFG11 (1/1000) in PBS containing 0.3% Triton X-100, washed, and then incubated with second antibody horse-radish peroxidase-conjugated goat anti-mouse IgG (1/1000) at room temperature for 60 min. Bound antibodies were visualized with an ECL western blotting detection kit (Amersham Biosciences, Foster City, CA). The membrane was reprobed with anti-β actin antibody after blocking with 5% fat-free dry milk in PBS containing 0.3% Triton X-100 solution once more.

For immunoprecipitation, 100 μg of proteins from the thalamus (extracted as above) was digested with chondroitinase ABC and then mixed with anti-KS 5D4 (5 μg) or anti-PTPζ antibody (2 μg) (6B4, a generous gift from N. Maeda and M. Noda) for 2 h at 4°C. The immune complex was precipitated with 30 μL of a 50% (v/v) suspension of protein A-sepharose (Amersham Biosciences) for 1 h at 4°C and washed three times with PBS containing 0.3% Triton X-100. The immunocomplexes bound to the protein A beads were isolated by centrifugation and were subjected to immunoblots.

Enzymatic treatment

Protein samples from the thalamus (extracted as above) were treated with keratanase I (Seikagaku; 5 mU/100 μg of protein, 0.1 M Tris–HCl, pH 7.3) or keratanase II (Seikagaku; 1 mU/μg of protein, 0.1 M sodium acetate, pH 6.5) for 4 h at 37°C. The immunoprecipitation samples were treated with chondroitinase ABC (Seikagaku; 1 mU/μg protein, 0.1 M Tris–acetate, pH 7.3) for 2 h at 37°C.

Controlled cortical stab injury and knife-cut injury

Six-week-old male C57BL6J mice were anesthetized and placed in a stereotaxic frame. Cortical injury was induced in the left parietal cortex. The cortical coordinates were 1.2 mm anterior and 1.0 mm lateral as to the bregma and a depth of 1 mm from the dura. A needle (1 mm in diameter) was lowered into the brain through a small burr hole drilled in the skull. For a knife-cut model, a knife cut (2.5 mm depth and 6.0 mm length) 1.0 mm lateral as to the bregma was made, and the lesions and the corresponding regions from normal mice were isolated 7 days after injury.

RT–PCR

A set of a forward primer (5′-AAGCCTACAGGTGGTGC GAA-3′) and a reverse primer (5′-CAGGACTGTTAAC CCGCTCA-3′) was used for RT–PCR for GlcNAc6ST-1 expression, and a set of a forward primer (5′-GGTGGAG GTCGGAGTCAACG-3′) and a reverse primer (5′-CAAAGTTGTCATGGATGACC-3′) were used for RT–PCR for GAPDH expression. SuperScript III reverse transcriptase (Invitrogen, Tokyo, Japan) was used to synthesize cDNA.

Morphometry

The midpoint of a lesion was determined by hematoxylin and eosin staining of several sections from serial 5-μm sections. To count reactive astrocytes, areas of specimens were traced, and 640 × 2200-μm^2 counting frames were selected by a computer-driven microscope stage (MetaMorph Offline version 6.3r2, Molecular Devices Corporation, Sunnyvale, CA) for counting of astrocytes around the lesions, and 216 × 100 μm^2 counting frames were selected for astrocytes accumulated in the lesion core. The accumulated astrocytes/total reactive astrocytes ratio was determined. The extents of extracellular matrix (ECM) and axonal outgrowth of the wound area were assessed by counting signals visualized on staining with anti-type IV collagen and SMI312 antibodies, respectively, for 640 × 2200-μm^2 counting frames around a lesion with the aid of computerized image analysis with the same soft program. Data were collected for at least three mice with each genotype in each experiment.

Statistical analysis

All data are presented as means ± SEM. Statistical analysis was performed with Student's *t*-test, and $p < 0.05$ was considered as being significant.

Acknowledgments

The authors thank M. Sawada for the critical comments on this study, A. Nitta for the advice regarding the operation of the cortical stab wound, and M. Noda and N. Maeda for the generous gift of the 6B4 antibody. K.U. is a research fellow of the Japan Society for the Promotion of Science. This work was supported by Grants-in-Aid from the Ministry of Education, Science, Sports, Culture (14082202 to T.M.; COEF01-09 to T.M. and K.K.).

Conflict of interest statement

None declared.

Abbreviations

BSA, bovine serum albumin; CNS, central nervous system; CS, chondroitin sulfate; ECA, *Erythrina cristagalli* lectin; ECM, extracellular matrix; FITC, fluoresceinisothiocyanate; GAP, growth-associated protein; GAPDH, glyceraldehyde-3-phosphate dehydrogenase; GFAP, glial fibrillary acidic protein; GlcNAc6ST, *N*-acetylglucosamine 6-*O*-sulfotransferase; KS, keratan sulfate; PBS, phosphate-buffered saline; PG, proteoglycan; PTP, protein tyrosine phosphatase; RT–PCR, reverse transcription–polymerase chain reaction; WT, wild type.

References

Akama, T.O., Nakayama, J., Nishida, K., Hiraoka, Y., Suzuki, M., McAuliffe, J., Hindsgaul, O., Fukuda, M., and Fukuda, M.N. (2001) Human corneal GlcNac 6-*O*-sulfotransferase and mouse intestinal GlcNac 6-*O*-sulfotransferase both produce keratan sulfate. *J. Biol. Chem.*, **276**, 16271–16278.

Akama, T.O., Nishida, K., Nakayama, J., Watanabe, H., Ozaki, K., Nakamura, T., Dota, A., Kawasaki, S., Inoue, Y., Maeda, N., and others (2000) Macular corneal dystrophy type I and type II are caused by distinct mutations in a new sulphotransferase gene. *Nat. Genet.*, **26**, 237–241.

Bradbury, E.J., Moon, L.D.F., Popat, R.J., King, V.R., Bennett, G.S., Patel, P.N., Fawcett, J.W., and Mcmahon, S.B. (2002) Chondroitinase ABC promotes functional recovery after spinal cord injury. *Nature*, **416**, 636–640.

Butler, C.D., Schnetz, S.A., Yu, E.Y., Davis, J.B., Temple, K., Silver, J., and Malouf, A.T. (2004) Keratan sulfate proteoglycan phosphacan regulates mossy fiber outgrowth and regeneration. *J. Neurosci.*, **24**, 462–473.

Cole, G.J. and McCabe, C.F. (1991) Identification of a developmentally regulated keratan sulfate proteoglycan that inhibits cell adhesion and neurite outgrowth. *Neuron*, **7**, 1007–1018.

Davies, S.J.A., Fitch, M.T., Memberg, S.P., Hall, A.K., Raisman, G., and Silver, J. (1997) Regeneration of adult axons in white matter tracts of the central nervous system. *Nature*, **390**, 680–683.

Dityatev, A. and Schachner, M. (2003) Extracellular matrix molecules and synaptic plasticity. *Nat. Rev. Neurosci.*, **4**, 456–468.

Dou, C.-L. and Levine, J.M. (1995) Differential effects of glycosaminoglycans on neurite growth on laminin and L1 substrates. *J. Neurosci.*, **15**, 8053–8066.

Fan, Q.W., Uchimura, K., Yuzawa, Y., Matsuo, S., Mitsuoka, C., Kannagi, R., Muramatsu, H., Kadomatsu, K., and Muramatsu, T. (1999) Spatially and temporally regulated expression of *N*-acetylglucosamine-6-*O*-sulfotransferase during mouse embryogenesis. *Glycobiology*, **9**, 947–955.

Filbin, M.T. (2003) Myelin-associated inhibitors of axonal regeneration in the adult mammalian CNS. *Nat. Rev. Neurosci.*, **4**, 1–11.

Fox, K. and Caterson, B. (2002) Freeing the brain from the perineuronal net. *Science*, **298**, 1187–1189.

Fukuda, M., Hiraoka, N., Akama, T.O., and Fukuda, M.N. (2001) Carbohydrate-modifying sulfotransferases: structure, function, and pathophysiology. *J. Biol. Chem.*, **276**, 47747–47750.

Grimpe, B. and Silver, J. (2004) A novel DNA enzyme reduces glycosaminoglycan chains in the glial scar and allows microtransplanted dorsal root ganglia axons to regenerate beyond lesions in the spinal cord. *J. Neurosci.*, **24**, 1393–1397.

Hemmerich, S., Bistrup, A., Singer, M.S., van Zante, A., Lee, J.K., Tsay, D., Peters, M., Carminati, J.L., Brennan, T.J., Carver-Moore, K., and others (2001) Sulfation of L-selectin ligands by an HEV-restricted sulfotransferase regulates lymphocyte homing to lymph nodes. *Immunity*, **15**, 237–247.

Horner, P.J. and Gage, F.H. (2000) Regenerating the damaged central nervous system. *Nature*, **407**, 963–970.

Jones, L.L. and Tuszynski, M.H. (2002) Spinal cord injury elicits expression of keratan sulfate proteoglycans by macrophages, reactive microglia, and oligodendrocyte progenitors. *J. Neurosci.*, **22**, 4611–4624.

Kawashima, H., Petryniak, B., Hiraoka, N., Mitoma, J., Huckaby, V., Nakayama, J., Uchimura, K., Kadomatsu, K., Muramatsu, T., Lowe, J.B., and Fukuda, M. (2005) *N*-acetylglucosamine-6-*O*-sulfotransferase-1 and -2 cooperatively control lymphocyte homing through L-selectin ligand biosynthesis in high endothelial venules. *Nat. Immunol.*, **6**, 1096–1104.

King, C.E., Canty, A.J., and Vickers, J.C. (2001) Alterations in neurofilaments associated with reactive brain changes and axonal sprouting following acute physical injury to the rat neocortex. *Neuropathol. Appl. Neurobiol.*, **27**, 115–126.

Kleene, R., and Schachner, M. (2004) Glycans and neural cell interactions. *Nat Rev. Neurosci.*, **5**, 195–208.

Lee, J.K., Bhakta, S., Rosen, S.D., and Hemmerich, S. (2000) Cloning and characterization of a mammalian *N*-acetylglucosamine-6-sulfotransferase that is highly restricted to intestinal tissue. *Biochem. Biophys. Res. Commun.*, **263**, 543–549.

Liesi, P. and Kauppila, T. (2002) Induction of type IV collagen and other basement-membrane-associated proteins after spinal cord injury of the adult rat may participate in formation of the glial scar. *Exp. Neurol.*, **173**, 31–45.

Maeda, N., Hamanaka, H., Oohira, A., and Noda, M. (1995) Purification, characterization and developmental expression of a brain-specific chondroitin sulfate proteoglycan, 6B4 proteoglycan/phosphacan. *Neuroscience*, **67**, 23–35.

McGee, A.W. and Strittmatter, S.M. (2003) The Nogo-66 receptor: focusing myelin inhibition of axon regeneration. *Trends Neurosci.*, **26**, 193–198.

McKeon, R.J., Jurynec, M.J., and Buck, C.R. (1999) The chondroitin sulfate proteoglycans neurocan and phosphacan are expressed by reactive astrocytes in the chronic CNS glial scar. *J. Neurosci.*, **19**, 10778–10788.

Miller, B., Sheppard, A.M., and Pearlman, A.L. (1997) Developmental expression of keratan sulfate-like immunoreactivity distinguishes thalamic nuclei and cortical domains. *J. Comp. Neurol.*, **380**, 533–552.

Moon, L.D., Asher, R.A., Rhodes, K.E., and Fawcett, J.W. (2001) Regeneration of CNS axons back to their target following treatment of adult rat brain with chondroitinase ABC. *Nat. Neurosci.*, **4**, 465–466.

Nilsson, B., Nakazawa, K., Hassell, J.R, Newsome, D.A., and Hascall, V.C. (1983) Structure of oligosaccharides and the linkage region between keratan sulfate and the core protein on proteoglycans from monkey cornea. *J. Biol. Chem.*, **258**, 6056–6063.

Properzi, F., Carulli, D., Asher, R.A., Muir, E., Camargo, L.M., van Kuppevelt, T.H., ten Dam, G.B., Furukawa, Y., Mikami, T., Sugahara, K., and others. (2005) Chondroitin 6-sulphate synthesis is up-regulated in injured CNS, induced by injury-related cytokines and enhanced in axon-growth inhibitory glia. *J. Neurosci.*, **21**, 378–390.

Roitbak, T. and Sykova, E. (1999) Diffusion barriers evoked in the rat cortex by reactive astrogliosis. *Glia*, **28**, 40–48.

Schnaar, R.L. (2003) Myelin molecules limiting nervous system plasticity. *Prog. Mol. Subcell. Biol.*, **32**, 125–142.

Scudder, P., Tang, P.W., Mehmet, H., and Feizi, T. (1986) Isolation and characterization of sulphated oligosaccharides released from bovine corneal keratan sulphate by the action of endo-beta-galactosidase. *Eur. J. Biochem.*, **157**, 365–73.

Seko, A., Dohmae, N., Takio, K., and Yamashita, K. (2003) β1,4-galactosyltransferase (β4GalT)-IV is specific for GlcNAc 6-*O*-sulfate. β4GalT-IV acts on keratan sulfate-related glycans and a precursor glycan of 6-sulfosialyl-Lewis X. *J. Biol. Chem.*, **278**, 9150–9158.

Seko, A. and Yamashita, K. (2004) β1,3-*N*-acetylglucosaminyltransferase-7 (β3Gn-T7) acts efficiently on keratan sulfate-related glycans. *FEBS Lett.*, **556**, 216–220.

Silver, J. and Miller, J.H. (2004) Regeneration beyond the glial scar. *Nat. Rev. Neurosci.*, **5**, 146–151.

Snow, D.M., Steindler, D.A., and Silver, J. (1990) Molecular and cellular characterization of the glial roof plate of the spinal cord and optic tectum: a possible role for a proteoglycan in the development of an axon barrier. *Dev. Biol.*, **138**, 359–376.

Stichel, C.C., Hermanns, S., Luhmann, H.J., Lausberg, F., Niermann, H., D'Urso, D., Servos, G., Hartwig, H., and Muller, H.W. (1999) Inhibition of collagen IV deposition promotes regeneration of injured CNS axons. *Eur. J. Neurosci.*, **11**, 632–646.

Uchimura, K., El-Fasakhany, F.M., Hori, M., Hemmerich, S., Blink, S.E., Kansas, G.S., Kanamori, A., Kumamoto, K., Kannagi, R., and

Muramatsu, T. (2002) Specificities of *N*-acetylglucosamine-6-*O*-sulfotransferases in relation to L-selectin ligand synthesis and tumor-associated enzyme expression. *J. Biol. Chem.*, **277**, 3979–3984.

Uchimura, K., Gauguet, J.M., Singer, M.S., Tsay, D., Kannagi, R., Muramatsu, T., von Andrian, U.H., and Rosen, S.D. (2005) PNAd and sialyl 6-sulfo Lex are eliminated in mice deficient in two high endothelial venule-expressed sulfotransferases. *Nat. Immunol.*, **6**, 1105–1113.

Uchimura, K., Kadomatsu, K., El-Fasakhany, F.M., Singer, M.S., Izawa, M., Kannagi, R., Takeda, N., Rosen, S.D., and Muramatsu, T. (2004) *N*-acetylglucosamine 6-*O*-sulfotransferase-1 regulates expression of L-selectin ligands and lymphocyte homing. *J. Biol. Chem.*, **279**, 35001–35008.

Uchimura, K., Muramatsu, H., Kadomatsu, K., Fan, Q.W., Kurosawa, N., Mitsuoka, C., Kannagi, R., Habuchi, O., and Muramatsu, T. (1998) Molecular cloning and characterization of an *N*-acetylglucosamine-6-*O*-sulfotransferase. *J. Biol. Chem.*, **273**, 22577–22583.

MOLECULAR AND CELLULAR BIOLOGY, Sept. 2006, p. 6923–6935 Vol. 26, No. 18
0270-7306/06/$08.00+0 doi:10.1128/MCB.02474-05

Solo/Trio8, a Membrane-Associated Short Isoform of Trio, Modulates Endosome Dynamics and Neurite Elongation

Ying-Jie Sun,[1,5]† Kaori Nishikawa,[1,3]† Hideki Yuda,[1] Yu-Lai Wang,[1] Hitoshi Osaka,[3] Nobuna Fukazawa,[1,4] Akira Naito,[5] Yoshihisa Kudo,[4] Keiji Wada,[1,7] and Shunsuke Aoki[1,2,6,7]*

Department of Degenerative Neurological Diseases[1] and Department of Demyelinating Disease and Aging,[2] National Institute of Neuroscience, NCNP, Kodaira, Tokyo 187-8502, Japan; Japan Science and Technology Agency (JST), Kawaguchi, Saiatama 332-0012, Japan[3]; Laboratory of Cellular Neurobiology, Tokyo University of Pharmacology and Life Science, Hachioji, Tokyo 192-0392, Japan[4]; Department of Anatomy and Structural Science, Yamagata University School of Medicine, Yamagata 990-9585, Japan[5]; New Energy and Industrial Technology Development Organization (NEDO), Kawasaki, Kanagawa 212-8554, Japan[6]; and JST, CREST, Kawaguchi, Saitama 332-0012, Japan[7]

Received 28 December 2005/Returned for modification 15 February 2006/Accepted 28 June 2006

With DNA microarrays, we identified a gene, termed *Solo*, that is downregulated in the cerebellum of Purkinje cell degeneration mutant mice. Solo is a mouse homologue of rat Trio8—one of multiple Trio isoforms recently identified in rat brain. Solo/Trio8 contains N-terminal sec14-like and spectrin-like repeat domains followed by a single guanine nucleotide exchange factor 1 (GEF1) domain, but it lacks the C-terminal GEF2, immunoglobulin-like, and kinase domains that are typical of Trio. Solo/Trio8 is predominantly expressed in Purkinje neurons of the mouse brain, and expression begins following birth and increases during Purkinje neuron maturation. We identified a novel C-terminal membrane-anchoring domain in Solo/Trio8 that is required for enhanced green fluorescent protein-Solo/Trio8 localization to early endosomes (positive for both early-endosome antigen 1 [EEA1] and Rab5) in COS-7 cells and primary cultured neurons. Solo/Trio8 overexpression in COS-7 cells augmented the EEA1-positive early-endosome pool, and this effect was abolished via mutation and inactivation of the GEF domain or deletion of the C-terminal membrane-anchoring domain. Moreover, primary cultured neurons transfected with Solo/Trio8 showed increased neurite elongation that was dependent on these domains. These results suggest that Solo/Trio8 acts as an early-endosome-specific upstream activator of Rho family GTPases for neurite elongation of developing Purkinje neurons.

Endosomal membrane trafficking in neurons plays a key role in various neural processes, including neurite elongation (19, 33), synaptic transmission (17), neuronal degeneration (36), and neuronal cell death or survival (7). The early endosome regulates the selective transfer of membrane proteins to other organelles, and thus it is a key organelle for sorting vesicles containing cell surface membrane proteins, including receptors, transporters, channels, and cell adhesion molecules (2, 29, 39, 47).

Several lines of evidence suggest that small GTPases play pivotal roles in regulating early-endosome dynamics (2, 39, 47). For example, Rab5 regulates the motility and fusion of early endosomes (32), whereas Rab4 and Rab5 control vesicle influx and efflux, respectively, in the early-endosome pool (28). Rho family GTPases also regulate early-endosome dynamics. Once such GTPase, Cdc42, controls endocytic transport in polarized cells (20), whereas RhoD specifically localizes to early endosomes and regulates their motility via diaphanous-related formin proteins (13). Upstream regulators of small GTPases that associate with early endosomes have been studied extensively. For example, early-endosome antigen 1 (EEA1) acts as an effector for Rab family small GTPases (5, 45). Although Rho family GTPases are also activated by multivalent upstream effectors (42), the specialized upstream activators that function in early endosomes remain unknown.

Trio, a member of the Dbl homology domain family of guanine nucleotide exchange factors (GEFs), was originally identified by its interaction with the leukocyte common antigen-related protein receptor (6). Trio has an N-terminal sec14-like domain, spectrin-like repeats, two GEF domains (GEF1 and GEF2), an immunoglobulin (Ig)-like domain, and a C-terminal Ser/Thr kinase domain (3). The GEF1 domain activates RhoG and Rac1, whereas GEF2 acts on RhoA, suggesting that Trio is involved in multiple GTPase cascades mediating various cellular processes (3). Genetic analysis of the Trio gene in *Drosophila* embryos implicates this protein in neuronal and retinal axon guidance (3). Mice lacking Trio die during embryogenesis and exhibit a loss of myofiber formation and cellular disorganization in the hippocampus and olfactory bulb (35). Although Trio is highly expressed in the adult brain, heart, liver, skeletal muscle, kidney, placenta, and pancreas (6), its effector function in these adult tissues remains unknown. Several Trio isoforms were recently identified (25), and the expression of each isoform was shown to be regulated in a tissue-specific manner. The functions of these isoforms, however, have not been delineated.

Purkinje cell degeneration (pcd) is an autosomal recessive

* Corresponding author. Mailing address: Department of Degenerative Neurological Diseases, National Institute of Neuroscience, National Center of Neurology and Psychiatry, 4-1-1 Ogawahigashi, Kodaira, Tokyo 187-8502, Japan. Phone: 81-42-346-1715. Fax: 81-42-346-1745. E-mail: aokis@ncnp.go.jp.
† Y.-J.S. and K.N. contributed equally to this work.

mutational disorder in mice that is characterized by degenerative loss of Purkinje neurons after postnatal day 15 (P15) to P18 (30). The causative mutation of pcd was identified at the *Nna1* locus (12). The disorder constitutes an adult-onset disease and presents mild phenotypes, thereby facilitating the analysis of cerebella that are nearly devoid of Purkinje neurons. Thus, the pcd mouse has been repeatedly used to screen for Purkinje neuron-specific genes, such as the gene encoding 28-kDa calbindin (34) or inositol 3-phosphate receptor 1 (IP3R) (24).

In this study, we used DNA microarrays to analyze gene expression in the cerebella of mice carrying a mutation governing pcd (30). We identified a Purkinje-predominant mouse cDNA encoding the protein Solo, which is a membrane-associated isoform of Trio. Amino acid sequence analysis showed that Solo is a homologue of the recently identified rat protein Trio8 (25). Solo/Trio8 specifically localized to early endosomes and regulated their dynamics. We also found that Solo/Trio8 modulated neurite morphology in primary cultured neurons. These data suggest that Solo/Trio8 is involved in the development of Purkinje neurons by affecting the dynamics of early endosomes.

MATERIALS AND METHODS

Animals. C57BL/6J-pcd mice were obtained from The Jackson Laboratory (Bar Harbor, ME). The cerebella of P24 pcd and wild-type (WT) mice were used for DNA microarrays. For SYBR green-based real-time quantitative reverse transcription (RT)-PCR, three cerebella were collected on each postnatal day. Animal care and handling were in accordance with institutional regulations for animal care and public law and were approved by the Animal Investigation Committee of the National Institute of Neuroscience, Japan.

DNA microarrays. Equivalent amounts of total RNA derived from each cerebellar sample were reverse transcribed into double-stranded cDNA that was then used as a template to synthesize biotin-labeled cRNA with the BioArray HighYield RNA transcription labeling kit (Enzo Diagnostics, Farmingdale, NY). Labeled cRNA was purified on RNeasy affinity resin (QIAGEN, Valencia, CA) and fragmented randomly to an average size of 50 to 100 bases by incubation in 40 mM Tris-acetate, pH 8.2, containing 100 mM K-acetate and 30 mM Mg-acetate at 94°C for 35 min. The labeled cRNA samples were analyzed with the Affymetrix murine genome U74A, -B, and -C array set (Affymetrix, Santa Clara, CA). Hybridization and array scanning were performed according to protocols provided by Affymetrix. Data analysis was performed with Microarray Suite software (Affymetrix).

5′ RACE. 5′ rapid amplification of cDNA ends (RACE) was performed with the 5′ RACE kit (Invitrogen, Carlsbad, CA) according to the manufacturer's protocol. First-strand cDNA was synthesized from cerebellar total RNA with a gene-specific primer (5′-AGAAACCAAAATGAGGCTGCTA-3′) corresponding to the cDNA sequence of expressed sequence tag (EST) clone AI587721. Nested PCR was performed to amplify DNA between the anchor primer and another primer (5′-TGAGGCTGCTAAGAATGGCTTGACTG-3′) specific for AI587721. The product (~1.2 kbp) displayed strong homology to the Trio cDNA sequence (GenBank accession no. NM_007118). A cDNA encoding the Solo/Trio8 open reading frame (ORF) was obtained by RT-PCR with primers 5′-TCTCGAGATGAAAGCTATGGATGTTTTGCC-3′ and 5′-AGAATTCGAATGGAAAGGTAAGGAAACTGAG-3′, derived from the human *Trio* gene (GenBank accession no. NM_007118) and the 1.2-kbp product, respectively. The resulting 5.6-kbp Solo/Trio8 DNA fragment was subcloned into the pGEM-T Easy vector (Promega, Madison, WI) for further sequencing.

In situ hybridization. In situ hybridization was performed as described previously (1). To synthesize cRNA probes for the *Trio* gene, the 357-bp fragment encoding part of the *Solo* gene (nucleotides [nt] 5134 to 5490; DDBJ accession no. AB106872; common probe) and a 339-bp noncoding part of the *Solo* gene (nt 5606 to 5944; *Solo*-specific probe) were subcloned into pBluescript-SKII (+) (Stratagene, La Jolla, CA).

SYBR green-based real-time quantitative RT-PCR. SYBR green-based real-time quantitative RT-PCR was performed with primers 5′-TCTCTCAGACACAGCCACGT-3′ (forward) and 5′-TGCTTCATATTAAGGGCAGCAG-3′ (reverse) to amplify Solo/Trio8 cDNA and primers 5′-AGAAGGTGGTGAAGCAGGCAT-3′ (forward) and 5′-ATCGAAGGTGGAAGAGTGGGA-3′ (reverse) for glyceraldehyde-3-phosphate dehydrogenase (GAPDH) cDNA. The quantitative RT-PCR method (user bulletin 2; Applied Biosystems, Foster City, CA) was modified to establish an expression level index for mRNA (1).

Plasmid constructs. With mouse cerebellar cDNA as a template, we performed PCR to construct plasmids encoding full-length (amino acids [aa] 1 to 1849) Solo/Trio8 tagged (N or C terminally) with enhanced green fluorescent protein (EGFP) and FLAG; Solo/Trio8 mutant constructs lacking the C-terminal transmembrane domain [Solo-TM(−) aa 1 to 1830; DDBJ accession no. AB106872] were prepared similarly. The primers used were 5′-CCGCTCGAGATGAAAGCTATGGATGTTTTGCC-3′ [forward primer for N- or C-terminally EGFP-tagged Solo and EGFP–Solo-TM(−)], 5′-GGAATTCGAATGGAAAGGTAAGGAAACTGAGC-3′ (reverse primer for EGFP-Solo), 5′-GGAATTCGCTTGTCATCCTGCGAGTCCGGCTGA-3′ [reverse primer for EGFP–Solo-TM(−)], 5′-CCGCTCGAGCGATGGACTACAAGGACGACGATGACAAGATGAAAGCTATGGATGTTTTGCCA-3′ [forward primer for N-terminally FLAG-tagged Solo and FLAG-Solo-TM(−)], 5′-GGGGGCGGCCGCTCAAATGGAAAGGTAAGGAAACT-3′ (reverse primer for N-terminally FLAG-tagged Solo), 5′-GGGGGCGGCCGCTCACTTGTCATCCTGCGAGTCCG-3′ [reverse primer for N-terminally FLAG-tagged Solo-TM(−)], 5′-CCGCTCGAGATGGATGAAAGCTATGGATGTTTTGC-3′ [forward primer for C-terminally FLAG-tagged Solo and FLAG-Solo-TM(−)], 5′-GGGGGCGGCCGCTTACTTGTCATCGTCGTCCTTGTAGTCAATGGAAAGGTAAGGAAACTGAGC-3′ (reverse primer for C-terminally FLAG-tagged Solo), 5′-GGGGGCGGCCGCTTACTTGTCATCGTCGTCCTTGTAGTCCTTGTCATCCTGCGAGTCCGGCTG-3′ [reverse primer for C-terminally FLAG-tagged Solo-TM(−)]. *Pfu* DNA polymerase was used for PCR, and the amplified products were cloned between the XhoI and EcoRI sites of pEGFP-C3/pEGFP-N1 (Clontech, Palo Alto, CA) or the XhoI and NotI sites of pCI-neo (Promega). To construct the GEF1-inactivated Solo mutant form Solo-AE, the mutations Gln^{1368} to Ala and Leu^{1376} to Glu were introduced into EGFP-Solo with the QuikChange site-directed mutagenesis kit (Stratagene) and primers 5′-CAAACCAGTTGCCCGGATAACAAAGTATCAGCTCGAGTTAAAGGAG-3′ and 5′-CTCCTTTAACTCGAGCTGATACTTTGTTATCCGGGCAACTGGT TTG-3′. All gene constructs were confirmed by DNA sequencing. Expression of the genes for Solo/Trio8 was controlled with a cytomegalovirus promoter.

Cell culture and transient transfections. COS-7, HEK293T, and NIH 3T3 cells were cultured at 37°C in 5% CO_2 in Dulbecco modified Eagle medium containing 10% fetal bovine serum, 100 U/ml penicillin, and 85 μg/ml streptomycin (Invitrogen). Cells were grown on 6- and 24-well or 100-mm dishes and four- and eight-well chamber slides and transfected with equal amounts (0.4 to 3.0 or 20 μg) of plasmid DNA per well with the Lipofectamine 2000 DNA transfection reagent (Invitrogen) according to the manufacturer's instructions and cultured for 8 to 24 h at 37°C.

Rac1 pull-down assay. COS-7 cells were cultured at a density of 2×10^6 cells per 100-mm dish and transfected with 20 μg of an EGFP-Solo expression construct or a control plasmid (pEGFP) as described above. After 16 h, cells were serum starved for 5 h and then washed with phosphate-buffered saline (PBS) and lysed in lysis buffer (25 mM HEPES, [pH 7.5], 150 mM NaCl, 1% [wt/vol] Igepal CA-630, 20 mM $MgCl_2$, 1 mM EDTA, 2% [wt/vol] glycerol, 1 mM Na_3VO_4, 25 mM NaF, complete EDTA-free protease inhibitor mixture [Roche Molecular Biochemicals, Indianapolis, IN]). Cell lysates were centrifuged at 20,000 × *g* for 20 min at 4°C. Rac1 activation was measured with the Rac1 activation assay kit (Upstate Biotechnology Inc., Lake Placid, NY) according to the manufacturer's instructions. Briefly, 0.5 ml of the supernatant (2 mg protein) was added to 10 μl of PAK1–p21–binding domain (PBD)–glutathione *S*-transferase–glutathione agarose beads (Upstate Biotechnology, Inc.), and the mixture was rotated for 1 h at 4°C, followed by three washes of the protein complexes with lysis buffer. PAK1-PBD-bound proteins were dissociated and denatured by boiling in Laemmli sample buffer and subjected to sodium dodecyl sulfate-polyacrylamide gel electrophoresis. The amount of active Rac1 (GTP-bound form) was analyzed by immunoblotting with a monoclonal antibody to Rac1 (Upstate Biotechnology, Inc.).

Cell fractionation. COS-7 cells were transfected with expression plasmids and cultured for 24 h. The cells were homogenized in 300 μl of ice-cold TNE buffer (50 mM Tris-HCl [pH 7.5], 150 mM NaCl, 1 mM EDTA) supplemented with protease inhibitors (Complete Protease Inhibitors; Roche Molecular Biochemicals) and sonicated for 30 s on ice. The homogenates were subjected to centrifugation at 20,000 × *g* for 30 min at 4°C. Supernatants (cytoplasmic fraction) were pooled, and pellets (including light membranes) were washed twice with 0.5 ml of TNE buffer and then lysed for 30 min on ice in radioimmunoprecipitation assay buffer (50 mM Tris-HCl [pH 7.5], 150 mM NaCl, 1 mM EDTA, 0.5%

sodium deoxycholate, 0.1% sodium dodecyl sulfate) with protease inhibitors and subjected to centrifugation at 20,000 × *g* for 30 min at 4°C.

Western blotting. Western blotting was performed as described previously (1). Blots were probed with antibodies to detect EGFP (anti-Living Colors A.v., JL-8; Clontech), anti-FLAG M2 (Sigma, St. Louis, MO), anti-Iκ-B (Cell Signaling Technology, Beverly, MA), anti-platelet-derived growth factor (PDGF) receptor α/β (Upstate Biotechnology, Inc.) or anti-β-actin (Sigma).

Neuronal cultures and transfections. Fetal C57BL/6J mice at embryonic day 16 (E16) were used for the primary culture of embryonic cortical neurons. The brain of each embryo was dissected from the overlying meninges, blood vessels, olfactory bulb, and hippocampus in Hanks' balanced salt solution (HBSS; Gibco, Gaithersburg, MD). Brains were minced with a 0.1-mm blade, and small pieces of the tissues were incubated in 0.25% trypsin–0.04% EDTA (Gibco) for 10 min at 37°C. Digestion was stopped by addition of 2% fetal bovine serum, and the mixture was incubated with 0.01% DNase I (Sigma) at room temperature for 2 min. After being spun down (5 min at 280 × *g*), neuronal cells were resuspended in HBSS. Single-cell suspensions were obtained by trituration and filtered through a 70-μm nylon cell strainer (BD, Bedford, MA) to remove undigested cell aggregates, followed by centrifugation for 5 min at 280 × *g*. Dispersed neurons were plated on Biocoat poly-D-lysine-coated four-well chamber slides (BD) at a density of 2×10^5 or 4×10^5 cells per well in Neurobasal medium (Invitrogen) containing B27 supplement (Invitrogen), penicillin-streptomycin (Invitrogen), and 2 mM L-glutamine (Invitrogen). The cultures were maintained at 37°C in a 5% CO_2 humidified incubator, and half of the medium volume was replaced with fresh medium about every 2 days. Cortical neurons were grown for 6 days in culture and then transfected as described above. For cotransfections, Lipofectamine 2000 reagent (4 μl) and DNA (a total of 1.6 μg of plasmids containing EGFP or EGFP-fused protein and DsRed [pDsRed Express-C1; Clontech] at a ratio of 8:1) were separately suspended in Opti-MEM (50 μl; Invitrogen) and gently combined. After a 20-min incubation at room temperature, the mixture (100 μl) was added to the culture medium (400 μl). DsRed is used to visualize the morphology of the transfected neurons (41). Neurons were allowed to express the transfected protein for 18 h, fixed with 4% formaldehyde in PBS, and immunostained with polyclonal anti-DsRed (1:10,000; rabbit IgG; BD) and mouse monoclonal anti-GFP 3E6 (1:2,000; Molecular Probes, Eugene, OR). Alexa Fluor dye-conjugated secondary antibodies (1:400; Molecular Probes) were used.

Immunofluorescence microscopy. Fluorescence immunostaining was performed as described previously (1). Dilutions of primary antibodies were as follows: anti-EEA1, anti-Bip/GRP78, and anti-GM130 (from BD Biosciences), all 1:100; anti-Rab5a and anti-Rab5b (Santa Cruz Biotech, Santa Cruz, CA), 1:200; anti-Rab7 (Santa Cruz Biotech), 1:100; anti-Tau1 and anti-Map2 (Chemicon International, Temecula, CA), 1:200; anti-calbindin D28k (Swant, Bellinzona, Switzerland), 1:500. All Alexa Fluor dye-conjugated secondary antibodies (Molecular Probes) were diluted 1:200. Immunofluorescence microscopy was performed with an ORCA-ER digital camera (Hamamatsu Photonics, Hamamatsu, Japan), and confocal microscopy was performed with the FLUOVIEW system (Olympus, Tokyo, Japan) or the Leica TCS SP2 spectral confocal scanning system (Leica Microsystems, Wetzlar, Germany) with a 20× objective lens, and images were acquired with Leica Confocal Software version 2.5.

Measurement of EEA1-positive vesicles. For analysis of early endosomes, the number of EEA1-positive vesicles in COS-7 cells expressing EGFP chimeras (and containing an intact nucleus stained with 4′,6′-diamidino-2-phenylindole [DAPI]) was quantified with Image-Pro Plus software version 4.5.1 (Media Cybernetics, Silver Spring, MD). EEA1-positive vesicles (>0.04 μm^2) were assayed by counting 40 cells. After we extracted the morphology of EEA1-positive endosomes with the object-extracting module of Image-Pro Plus, the clustered vesicles were separated with the Watershed Split module in the software. These data were statistically analyzed with Prism software version 3.0c (GraphPad, San Diego, CA). The data were statistically evaluated with one-way analysis of variance, followed by Bonferroni's test.

Endocytosis. Transferrin or Sulforhodamine 101 uptake was assessed as described previously (14, 50). Briefly, COS-7 cells were transfected with EGFP or EGFP-Solo constructs by using Lipofectamine 2000. Seven hours after transfection, the cells were depleted of bovine transferrin by incubation for 45 min in Dulbecco modified Eagle medium containing 0.1% bovine serum albumin and then labeled with human transferrin fluorescently labeled with Alexa-594 (Molecular Probes) at 25 μg/ml or with the fluid-phase fluorescent marker Sulforhodamine 101 (Molecular Probes) at 25 μg/ml for 15 min at 37°C. Internalization was then stopped by placing the cells on ice and washing them three times with ice-cold PBS before formaldehyde fixation. For analysis of endocytosis, fluorescence of Alexa-594-labeled transferrin or Sulforhodamine 101 in COS-7 cells expressing EGFP-Solo chimeras was quantified with Image-Pro Plus software version 4.5.1 with the density histogram module.

Cortical neuron morphometry and analysis. Images of immunostained neurons as described above were captured with an ORCA-ER digital camera, and morphometric analysis of the neurites and their branching was performed with Kurabo Neurocyte Image Analyzer software version 1.5 (KURABO, Osaka, Japan). To analyze the effects on neurite morphology, EGFP-positive cells were assayed by counting at least 60 cells from randomly selected fields. All neurites were measured irrespective of whether they were axons. Neuronal morphology was assessed according to four criteria, pass (number of branches), joint (number of branch points), total length (axon-and-dendrite length), and average maximum neurite length (axon length; Tau1 immunohistochemistry showed that the longest neurite of E16 mouse-derived embryonic cortical neurons was an axon; data not shown). The data were statistically evaluated by one-way analysis of variance, followed by Bonferroni's test.

Organotypic slice culture. The method used for slice culture has been described previously (49). In brief, C57BL/6J mice were decapitated and their brains were dissected and sliced in ice-cold HBSS with a vibratome. P11 cerebella were sliced coronally at a 200-μm thickness. Slices were transferred onto Millicell-CM inserts (Millipore, Bedford, MA) and cultured at the air-medium interface in 5% CO_2 in air at 37°C. Cerebellar slices were cultured essentially as described before (48), in a medium which consisted of 15% heat-inactivated horse serum (Invitrogen), 25% Earle's balanced salt solution (Sigma), 60% Eagle's basal medium (Invitrogen), 5.6 g/liter glucose, 3 mM L-glutamine, 20 nM progesterone, 1 mM sodium pyruvate, 100 U/ml penicillin, 100 μg/ml streptomycin, and Sigma I-1884 supplement (giving final concentrations of 5 μg/ml insulin, 5 μg/ml transferrin, and 5 ng/ml sodium selenite). At 1 day in vitro, cerebellar slices were transfected with small interfering RNA (siRNA).

Transfection of siRNA. We used siRNA to knock down Solo/Trio8 expression in cerebellar-slice cultures. A 21-oligonucleotide siRNA duplex was designed by the siDirect program (RNAi Co., Ltd., Tokyo, Japan). The siRNA oligonucleotide sequences that were used to target the C-terminal transmembrane domain in Solo/Trio8 (region, bp 5483 to 5505) were 5′-GACAAGCAUUACGUUGAUUUG-3′ (sense) and 5′-AAUCAACGUAAUGCUUGUCAU-3′ (antisense) and were synthesized by RNAi Co., Ltd. For the control, scrambled siRNA, silencer negative control no. 1 siRNA (proprietary sequence; Ambion, Austin, TX) was used. To confirm the siRNA effect, the EGFP-Solo plasmid and siRNA targeting Solo/Trio8, as well as a scrambled siRNA control, were cotransfected into COS-7 cells with Lipofectamine 2000 according to the manufacturer's instructions. After 24 h, significant siRNA-mediated suppression of Solo/Trio8 expression was detected by immunocytochemistry with anti-GFP monoclonal antibody 3E6 to estimate the fluorescence intensity of EGFP-expressing cells by fluorescence microscopy. For analysis of the inhibitory efficiency of siRNA, fluorescence signals in COS-7 cells expressing EGFP-Solo were quantified with Image-Pro Plus software version 4.5.1 with the density histogram module. To knock down endogenous Solo/Trio8 expression in Purkinje cells, at 1 day in vitro the siRNA was transfected into cerebellar slices with X-tremeGENE siRNA Transfection Reagent (Roche Applied Science) according to the manufacturer's instructions. In addition, scrambled siRNA no. 1 was transfected as a negative control. After 2 days, the slices were immunostained with anti-calbindin D28k as described below.

Immunohistochemistry. For Purkinje neuron morphometry, Purkinje cells were visualized by immunostaining with a mouse monoclonal antibody against calbindin D28k. The immunostaining method for brain slices has been described previously (48). Briefly, slices were fixed in 4% paraformaldehyde in PBS for 1 h at room temperature and washed three times with PBS. Slices were incubated with 10% normal goat serum in PBS containing 0.3% Triton X-100 for 1 h. Slices were then incubated overnight at 4°C with primary antibody diluted 1:500 in PBS containing 3% normal goat serum and 0.3% Triton X-100 and then washed three times with PBS. Slices were incubated with goat Alexa 488-conjugated secondary antibody diluted 1:200 in PBS containing 1% goat serum and 0.3% Triton X-100 for 1 h at room temperature and washed three times with PBS. Images of immunostained Purkinje neurons were captured with the Leica TCS SP2 spectral confocal scanning system (20× objective lens), and morphometric analysis of the axons was performed with the Kurabo Neurocyte Image Analyzer as described above.

Nucleotide sequence accession number. The nucleotide sequence of mouse Solo/Trio8 has been deposited in the DDBJ nucleotide sequence database under accession number AB106872.

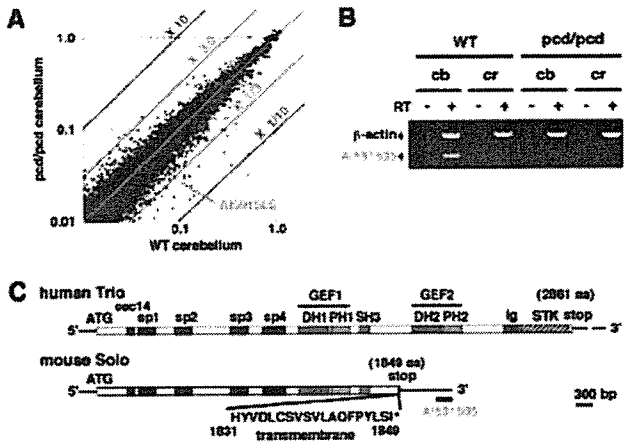

FIG. 1. Identification of a cDNA sequence predominantly expressed in Purkinje neurons. (A) Scattergram analysis of microarray data. Cerebellar cDNAs derived from pcd and WT mice were analyzed with DNA microarrays, and the average signal from each gene was normalized to the GAPDH signal and plotted to yield the scattergram. The AI591505 cDNA is indicated on the plot. (B) RT-PCR analysis of AI591505 transcript expression in the cerebella (*cb*) and cerebra (*cr*) of pcd and WT mice, respectively. PCRs for the β-actin gene (internal control) and AI591505 were performed in a single tube. (C) Structural relationship between the gene for Solo/Trio8 and a consensus of human Trio genes. Protein domains are indicated within the bars, and the 5′ and 3′ noncoding regions are indicated by horizontal lines. The domains shown are as follows: sec14, sec14p-like putative lipid binding domain; sp, spectrin-like domain; DH, Dbl homology domain; PH, pleckstrin homology domain; SH3, Src homology 3 domain; Ig, Ig-like domain; STK, serine/threonine kinase domain.

RESULTS

DNA microarray analysis of the pcd mouse cerebellum. Since no exhaustive gene expression analysis of the pcd mouse has been reported to date, we evaluated changes in cerebellar gene expression from P24 pcd mice (with 70 to 80% Purkinje neuronal loss) and WT mice with DNA microarrays containing almost 6,000 characterized genes and 30,000 ESTs. A comparison between two pcd mice and two WT mice revealed pcd-specific variability in gene expression (Fig. 1A). A scattergram constructed from hybridization data of 12,518 highly expressed genes (those having signals >0.01% of that measured for GAPDH) revealed only six upregulated genes (>3-fold) and 26 downregulated genes (<0.33-fold) in pcd mice (Table 1).

EST AI591505 is expressed exclusively in Purkinje neurons. Among the downregulated genes, we identified uncharacterized EST clone AI591505 (GenBank) (Fig. 1A; Table 1). AI591505 is 236 bp in length and has no homology with any annotated genes. The as-yet-uncharacterized AI591505 transcript was highly expressed in the normal mouse cerebellum (~10% of the GAPDH signal in the WT array; Fig. 1A). AI591505 was of interest because its decreased expression level in the pcd cerebellum suggested that it is a relatively highly expressed uncharacterized Purkinje neuron-specific gene. The decreased expression of the AI591505 transcript in the pcd cerebellum was confirmed by RT-PCR analysis with the cerebra and cerebella of pcd and WT mice, respectively. This transcript was expressed predominantly in the cerebellum, and expression in the pcd mouse was clearly lower than in the WT mouse (Fig. 1B). In situ hybridization showed that the transcript was expressed predominantly in the WT Purkinje cell layer at P24 (Fig. 2B) but not in the E16 brain (Fig. 2A) and was decreased in pcd Purkinje cells (Fig. 2B, c to i). Relatively low-level expression was also detected in the olfactory bulb and hippocampus (Fig. 2B, c to e). The expression level of the AI591505 gene in the P7 pcd cerebellum (before onset of degenerative loss of Purkinje neurons) was equivalent to that in the P7 WT cerebellum (data not shown), although the *Nna1* (pcd causative gene) expression level was significantly decreased in the P7 pcd cerebellum (data not shown), suggesting that the AI591505 gene is not a downstream gene directly controlled by *Nna1* expression.

Identification of Solo/Trio8, a Trio splice variant, expressed predominantly in Purkinje neurons. An additional search of databases identified another EST, AI587721, containing a region overlapping the AI591505 sequence. 5′ RACE with the AI587721 sequence yielded a 1.2-kbp cDNA clone from the cerebellum. A search of GenBank revealed that this clone contained a part of the *Trio* sequence (accession no. NM_007118). To clone the entire ORF, a PCR was performed with primers for *Trio* (forward) and the cDNA clone (reverse)

TABLE 1. Genes with altered expression in the pcd cerebellum

Gene (accession no.)	Relative expression		pcd/WT ratio
	WT[a]	pcd[a]	
Genes upregulated in pcd cerebellum			
CPP32 (U63720)	0.042	0.137	3.29
TYRO (AF024637)	0.027	0.088	3.25
Slp-w7 (X06454)	0.024	0.082	3.45
UN[b] (AK084804)	0.015	0.046	3.08
UN[b] (BC055829)	0.014	0.043	3.00
DnaJ-like (AK053156)	0.011	0.036	3.37
Genes downregulated in pcd cerebellum			
IP3R1 (X15373)	0.533	0.054	0.10
28-kDa calbindin (D26352)	0.525	0.032	0.06
NK6 (AK083449)	0.396	0.113	0.29
PCP-1 (M21530)	0.356	0.040	0.11
RGS8 (AK044337)	0.322	0.084	0.26
GluR1 (BC056397)	0.299	0.098	0.33
PCP-2 (M21532)	0.298	0.056	0.19
DRR1-like (AK032875)	0.162	0.040	0.24
Ca^{2+}-ATPase (BC026147)	0.146	0.019	0.13
PKC-γ (L28035)	0.135	0.024	0.18
EAAC4 (D83262)	0.131	0.017	0.13
MGF (M57647)	0.129	0.031	0.24
Delphilin (AF099933)	0.127	0.013	0.10
rp S18a (AB049953)	0.114	0.031	0.27
AI591505	0.094	0.028	0.30
Tubulin ligase (AB093278)	0.087	0.014	0.16
Metalloprotease (AK034528)	0.074	0.023	0.31
Shank2 (AB099695)	0.066	0.019	0.28
PH protein (AK028383)	0.060	0.013	0.22
NSC dendrite regulator (BC030853)	0.056	0.017	0.31
Aspartate-β-hydroxylase (AF289488)	0.056	0.017	0.31
Ca^{2+} channel α1G (AJ012569)	0.055	0.011	0.20
Tm4sf10 (BC019751)	0.049	0.015	0.31
Chemokine (AY241872)	0.039	0.013	0.32
Oxytocin-neurophysin I (M88355)	0.038	0.011	0.28
ARM repeat protein (AK044219)	0.033	0.010	0.30

[a] Expression level relative to GAPDH (average from two WT or pcd mice).
[b] UN; uncharacterized gene.

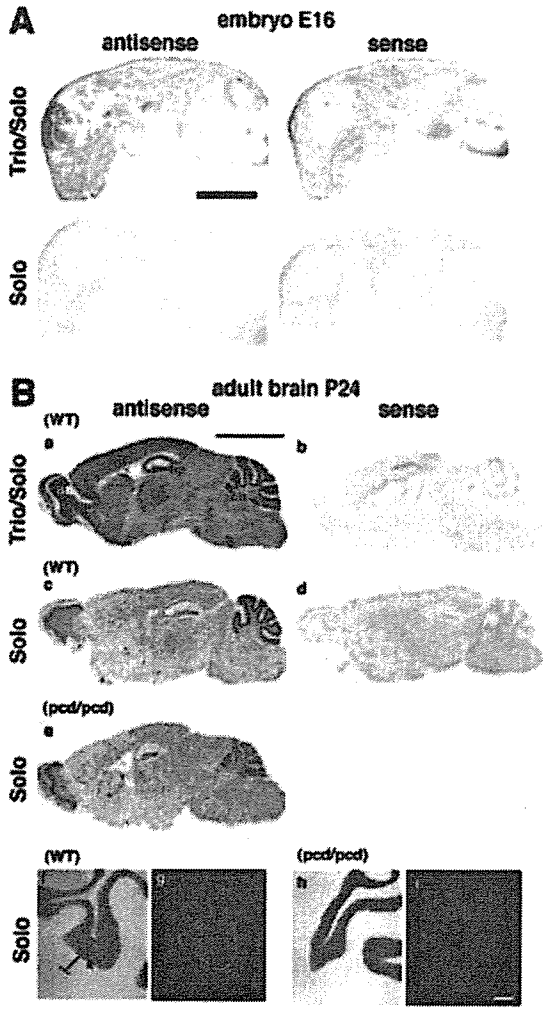

FIG. 2. Expression of Solo and Trio mRNAs in the mouse embryo and adult mouse brain. (A) In situ hybridization analysis of the mouse embryo (E16) with Solo-specific and Solo/Trio-common cRNA probes. Antisense and sense probes were prepared with Solo-specific and Solo/Trio (common to both) regions of the cDNA, respectively, and hybridized with tissue sections from an E16 mouse whole embryo. Bar = 5 mm. (B) In situ hybridization analysis of Solo transcript (AI591505) in P24 WT (a to d, f, g) and pcd (e, h, i) brains. Antisense and sense probes were prepared from Solo-specific and Solo/Trio (common to both) regions of the cDNA, respectively, and hybridized with tissue sections from P24 mouse whole brains. Regions in part a are labeled as follows: cb, cerebellum; ctx, cortex; hp, hippocampus; ob, olfactory bulb. The arrow in part f indicates the Purkinje cell layer, and the bars in part f indicate the molecular (lower) and granule (upper) layers. Bar in part a = 5 mm (same scale for parts a to e). Bar in part i = 200 μm (same scale for parts f to i).

to yield a cDNA with an entire ORF of 5,550 bp encoding 1,849 aa (Fig. 1C) from the cerebellum. The human *Trio* ORF contains 8,586 bp encoding 2,861 aa (6) (Fig. 1C); the cloned cDNA lacked the region between nucleotides 5491 and 8586 but contained a distinct 874-bp sequence at the 3′ end (Fig. 1C). A search of GenBank revealed the corresponding exon in the mouse *Trio* gene (data not shown), suggesting that the transcript is an alternatively spliced product of the *Trio* gene. We thus named this isoform Solo, for *s*hort-form sp*l*ice variant of Tri*o*. Solo contains an N-terminal sec14-like domain, spectrin-like repeats, a GEF1 domain, one SH3-like domain, and the unique C-terminal hydrophobic sequence HYVDLCSVS VLAQFPYLSI (aa 1831 to 1849, Fig. 1C). Computational analyses with a protein motif search program (http://motif.genome.ad.jp/) suggested that this C-terminal hydrophobic sequence resembles transmembrane helices of G-protein-coupled receptors (data not shown). McPherson et al. recently reported identification of rat Trio variants (25). Among them, the amino acid sequence of rat Trio8 was highly similar (99.7%) to that of mouse Solo, suggesting that Solo is a mouse homologue of Trio8.

To delineate the expression patterns of the genes for Solo/Trio8 and Trio in the mouse brain, we performed in situ hybridization with Solo-specific and Solo/Trio-common cRNA probes. The Solo/Trio-common probe signal was distributed over the entire mouse brain, and more-intense signals were observed in the hippocampus, olfactory bulb, cortical layers, and cerebellum (Fig. 2B, a and b). This hybridization pattern differed from that of the Solo-specific probe, which was predominantly expressed in the Purkinje cell layer of the cerebellum (Fig. 2B, c, d, f, and g). To determine if Solo/Trio8 mRNA is actually translated into protein, we performed Western blot analysis with a polyclonal antibody recognizing a 14-aa internal sequence near the N terminus of Solo and Trio (anti-Solo/Trio antibody). The immunoblot showed a 210-kDa immunoreactive band in the mouse cerebellum, in good agreement with the expected molecular mass of Solo (212 kDa) (data not shown). McPherson et al. (25) also detected a 210-kDa rat Trio8 protein in the rat cerebellum by Western blotting with an antibody against Trio8. The size of the Solo/Trio8 protein in mouse and rat cerebella was identical to that measured in COS-7 cells transfected with the Solo expression vector (Fig. 3C). Our antibody against Solo/Trio did not work well in immunohistochemical, immunocytochemical, and fractionation experiments (data not shown), so we were unable to determine the protein expression pattern in the brain.

Guanine nucleotide exchange activity of Solo/Trio8 for a Rho family GTPase. The GEF1 domain of Trio activates RhoG and Rac1, whereas GEF2 acts on RhoA (3). We addressed whether the GEF1 domain of Solo/Trio8 has guanine nucleotide exchange activity for Rac1 by a pull-down assay with the PBD of PAK1, which specifically binds to GTP-bound Rac1 (active form) but not to the inactive GDP-bound form (4). The amount of activated Rac1 in COS-7 cells transfected with the EGFP-Solo construct was markedly increased compared with that in negative control cells transfected with EGFP (Fig. 3B, top). Previous studies demonstrated that a double amino acid mutant form of Trio (Q1368A and L1376E within the GEF1 domain) completely abolishes the GEF1 activity (10, 23). The Q1368A and L1376E double mutation (EGFP–Solo-AE, Fig. 3A) abolished EGFP-Solo-mediated Rac1 activation in COS-7 cells (Fig. 3B, top). The C-terminal hydrophobic sequence (HYVDLCSVSVLAQFPYLSI; Fig. 1C) of Solo/Trio8 was predicted by a protein motif search program to function as a membrane-anchoring domain (data not shown). Deletion of this putative domain (EGFP–Solo-TM(−), Fig. 3A) did not affect Rac1 activation (Fig. 3B, top). There was no significant difference in the total amount of Rac1 expressed in COS-7 cells transfected with the EGFP, EGFP-Solo, EGFP–

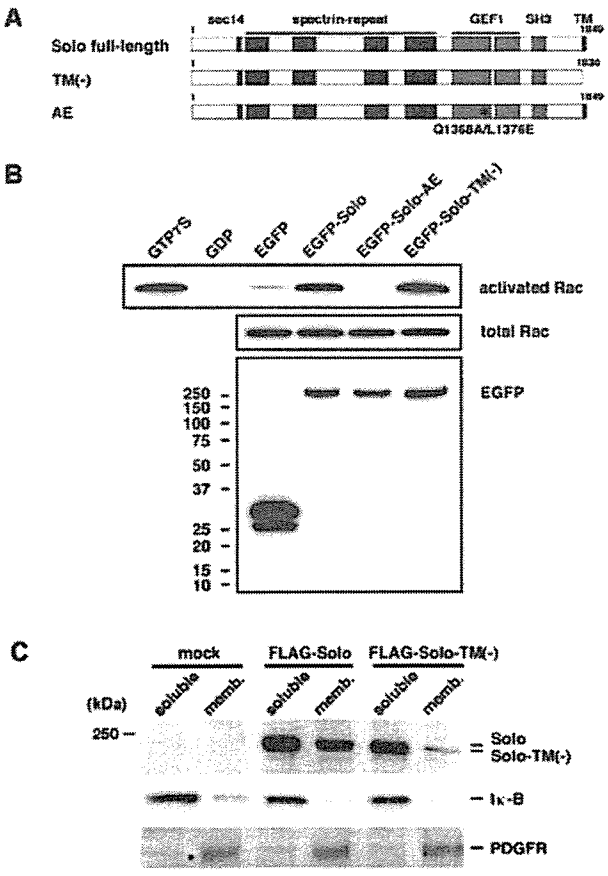

FIG. 3. GEF activity of Solo/Trio8 and localization in cellular membranes. (A) Schematic representation of full-length, C-terminally truncated Solo-TM(−) and AE mutant (GEF inactive; Q1368A/L1376E). (B) Rac1 activation by the GEF1 activity of Solo/Trio8. EGFP, EGFP-Solo, EGFP–Solo-AE, and EGFP–Solo-TM(−) were transiently expressed in COS-7 cells. Cells were cultured for 24 h and then serum starved for an additional 5 h prior to the Rac1 activation assay. PBD-bound Rac1 protein was pulled down and analyzed by Western blotting with monoclonal anti-Rac1. (Top) GTP-bound Rac1 (active form). Cell lysates treated with GTPγS or GDP served as the respective positive and negative controls. (Middle) Total cell lysates probed for Rac1 demonstrate equal amounts of total Rac1 in all transfected cells. (Bottom) Expression of transfected proteins was evaluated by Western blotting with anti-GFP. The values on the left are molecular sizes in kilodaltons. (C) COS-7 cells were transfected with pCI-neo (mock), pCI-neo-FLAG-Solo, or pCI-neo-FLAG-Solo-TM(−). Soluble and membrane proteins were subjected to sodium dodecyl sulfate-polyacrylamide gel electrophoresis and immunoblotted with anti-FLAG, anti-Iκ-B (soluble-protein control), or anti-PDGF-Rα/β (membrane protein control). (D) Fluorescence microscopy of cells transfected with N- or C-terminally EGFP- or FLAG-tagged Solo or C-terminally truncated Solo-TM(−) expression constructs. Expression constructs encoding N-terminally EGFP-tagged Solo and Solo-TM(−) were transfected into COS-7 cells (a, b). Expression constructs of C-terminally FLAG-tagged Solo and Solo-TM(−) were transfected into COS-7 cells and stained with anti-FLAG (c, d). EGFP alone, C-terminally EGFP-tagged Solo, and Solo-TM(−) mutant expression constructs were transfected into NIH 3T3 cells (e to g). Bars = 10 μm.

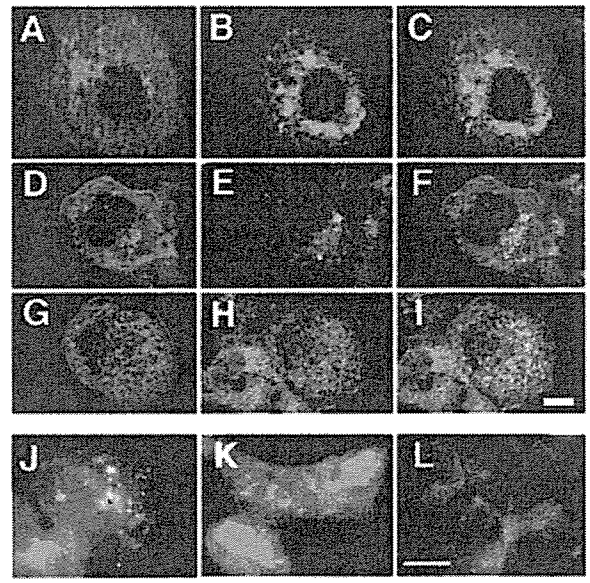

FIG. 4. Subcellular localization of Solo/Trio8. An EGFP-tagged Solo/Trio8 expression construct (green) was transfected into COS-7 cells (A, D, and G). COS-7 cells were further stained (red) with anti-Bip/GRP78 (B), anti-GM130 (E), or anti-EEA1 (H). Merged images are indicated to the right in each row (C, F, and I). Images were obtained by confocal microscopy. The EGFP-tagged Solo/Trio8 expression construct was transfected into 293 cells, and EGFP staining (green) was assessed. The 293 cells were further stained (red) for specific markers with anti-Rab5a (J), anti-Rab7 (K), or anti-Rab11 (L). Merged images are indicated, and colocalization is shown in yellow (blue arrowheads in J). Images were obtained with a charge-coupled device camera. Bars = 5 μm.

Solo-AE, or EGFP–Solo-TM(−) expression construct (Fig. 3B, middle). Furthermore, the amount of EGFP-Solo did not differ between COS-7 cells transfected with WT or mutant Solo constructs (Fig. 3B, bottom).

Solo/Trio8 localizes to early endosomes. To address whether the potential C-terminal membrane-anchoring domain of Solo/Trio8 is required for membrane association, N-terminally FLAG-tagged Solo and Solo-TM(−) expression constructs (Fig. 3A) were transfected into COS-7 cells and the cell lysates

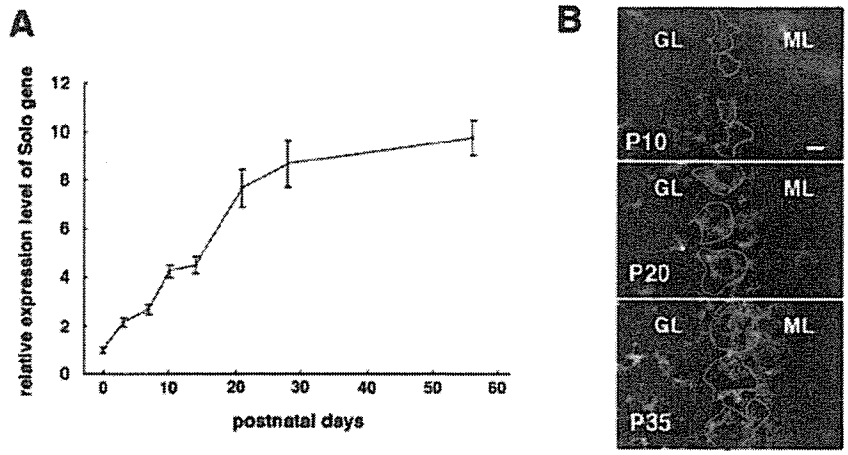

FIG. 5. Expression profile of Solo/Trio8 and the increase in the number of early endosomes during postnatal mouse cerebellar development. (A) SYBR green-based quantitative RT-PCR analysis of Solo/Trio8 transcript in WT mouse cerebellum during postnatal development. Expression levels are relative to P0 (P0 = 1.0). Each bar represents the mean ± the standard error of the mean (n = 3; three cerebella). (B) Immunohistochemistry of cerebellum sections during stages of postnatal maturation of Purkinje neurons (P10, P20, and P35). A section (20 μm) was obtained from a C57BL/6J mouse brain. Sections were stained with anti-calbindin and coimmunostained with anti-EEA1. Merged images are shown in gray. Green lines indicate the location of each cell body of calbindin-positive Purkinje neurons. Bright, dot-like signals indicate EEA1-positive early endosomes. GL, granule cell layer; ML, molecular cell layer. Bar = 20 μm

were analyzed by Western blotting. N-terminally FLAG-tagged Solo was a single band of ~220 kDa that localized to both soluble and membrane fractions (Fig. 3C). Nearly all of the N-terminally FLAG-tagged Solo-TM(−) was found in the soluble fraction (Fig. 3C), indicating that the C-terminal domain is essential for membrane anchoring. The internal control proteins IκB (soluble) and PDGF receptor α/β (membrane associated) were detected in the appropriate fractions (Fig. 3C). The subcellular localization of Solo was confirmed by immunofluorescence microscopy of N- or C-terminally EGFP- or FLAG-tagged Solo constructs. The N-terminally tagged construct displayed a pattern consistent with localization to the cytoplasm and to small vesicles in COS-7 cells (Fig. 3D, a; Fig. 4A, D, and G), 293 cells (Fig. 4J to L), and primary cultured neurons (see Fig. 7D). The C-terminally tagged protein yielded similar results (Fig. 3D, c, COS-7; Fig. 3D, f, NIH 3T3). N-terminally and C-terminally EGFP- or FLAG-tagged Solo-TM(−) displayed uniform cytoplasmic localization (Fig. 3D, b, d, and g). These results indicated that the putative C-terminal membrane-anchoring domain is essential for vesicular localization. Although various N-terminally truncated Solo mutant constructs generated by serial deletion of N-terminal domains, including the sec14-like and spectrin-repeat domains, also failed to distribute to vesicles, Western blotting revealed that these mutant proteins were not stable in COS-7 cells (data not shown).

Subcellular localization of Solo/Trio8 was then analyzed with organelle-specific markers. Antibodies against Bip/GRP78, GM130, and EEA1 specifically label the endoplasmic reticulum (22, 31), Golgi (1), and early endosomes (5, 9), respectively (Fig. 4B, E, and H). Of these markers, only the signal for the early-endosome marker EEA1 partially overlapped the EGFP-Solo signal (Fig. 4A to I), suggesting that Solo/Trio8 localizes to early endosomes. To confirm the localization with other endosomal markers and another cell type, we stained EGFP-Solo-expressing 293 cells with specific antibodies to Rab5 for early endosomes (28), Rab7 for late endosomes (11), and Rab11 for recycling endosomes (40). EGFP-Solo staining partially overlapped Rab5-positive vesicles (Fig. 4J) but not Rab7- or Rab11-positive vesicles (Fig. 4K and L). These data indicated that Solo/Trio8 localizes to early endosomes. However, at this level of resolution, we could not rule out the possibility that the observed colocalization of Solo with EEA1 and Rab5 arose from coincidental overlap due to the high-density punctate staining resulting from overexpression of these proteins.

We could not define which subclass of early endosomes expressed Solo/Trio8 because specific markers for such a classification are not available.

Solo/Trio8 gene expression correlates with early-endosome maturation levels in postnatal Purkinje neuronal cells. We analyzed the temporal pattern of the Solo/Trio8 gene expression level during Purkinje neuron maturation after birth (Fig. 5A). Analysis of mRNA samples prepared from P0 to P56 cerebella showed that the gene for Solo/Trio8 was expressed after birth, markedly increased during the first 4 weeks of life, and achieved maximal levels during adulthood. To investigate the development of early endosomes in Purkinje neurons, we stained cerebellar brain sections with antibodies against EEA1 and calbindin D28k (Purkinje neuron marker) (34). The number of large EEA1-positive early endosomes increased in Purkinje neurons during the postnatal maturation stage after P20 (Fig. 5B), indicating a correlation between expression levels of Solo/Trio8 and early-endosome development in D28k-positive Purkinje neurons.

Solo/Trio8 modulates early-endosome dynamics via its GEF1 activity and C-terminal membrane-anchoring domain. We assessed the effect of Solo overexpression on EEA1-positive early endosomes in COS-7 cells. The average number of EEA1-positive early endosomes increased in EGFP-Solo-expressing cells (1.84-fold ± 0.217-fold versus EGFP alone; $P <$ 0.001, n = 40; Fig. 6A and B). We next addressed whether

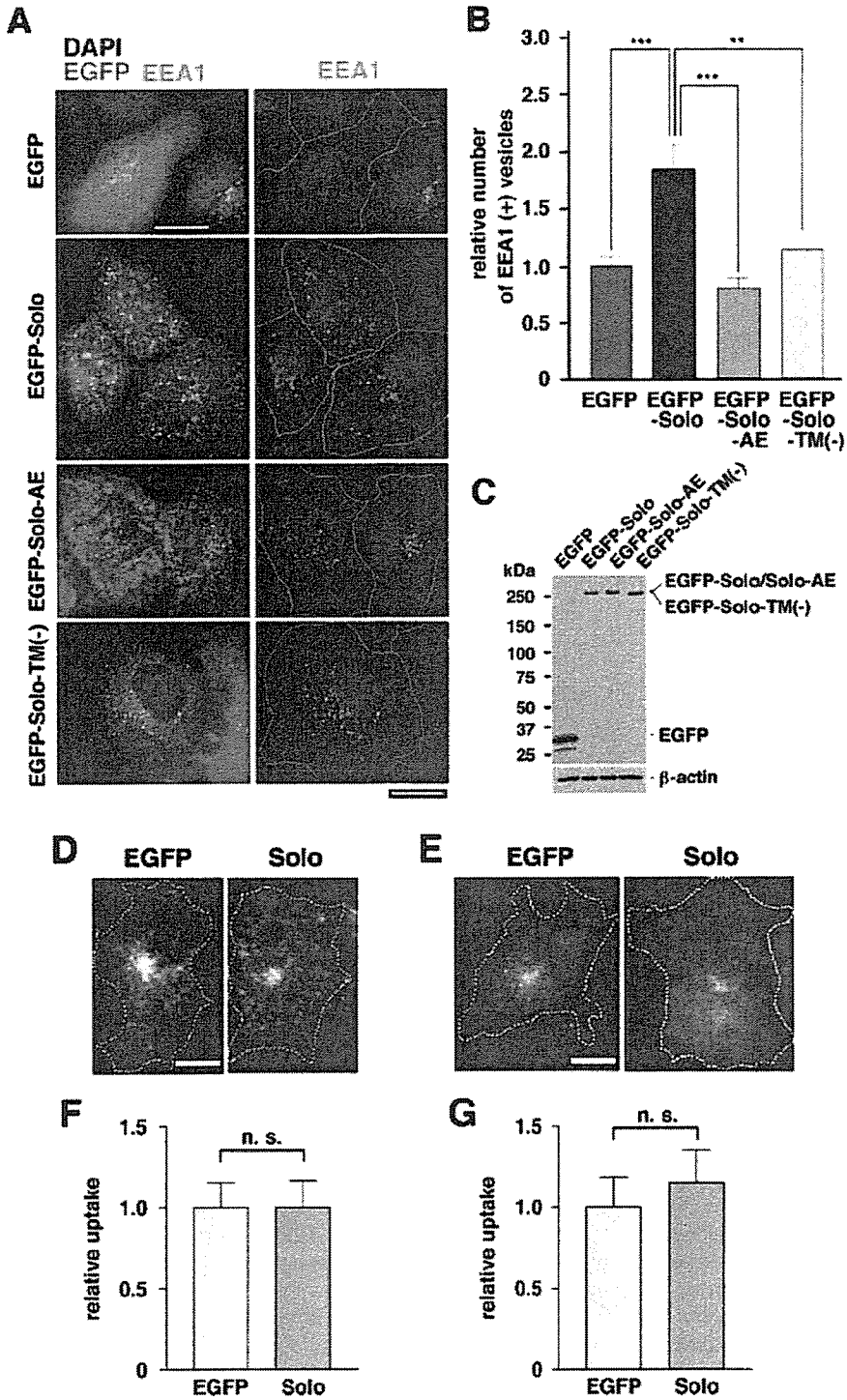

FIG. 6. Solo/Trio8 modulates early-endosome dynamics. (A) Expression constructs of the control EGFP, EGFP-Solo, EGFP–Solo-AE (GEF1 inactive form), and EGFP–Solo-TM(−) were transfected into COS-7 cells (EGFP signal is indicated in green). At 8 h posttransfection, cells were stained with anti-EEA1 (red) and DAPI (blue). Merged tricolor images are shown to the left. For ease of visualization, two-color images (minus the green EGFP signal) are shown to the right. Dotted lines indicate cellular edges. Images were obtained with a cooled charge-coupled device camera. Bars = 10 μm. (B) Quantification of EEA1-positive vesicles (early endosomes; survey square, >0.04 μm^2) in COS-7 cells transfected with Solo/Trio8 expression constructs. The number of early endosomes counted for each construct is presented relative to that determined for EGFP-expressing cells (negative control; EGFP = 1.0). Each bar represents the mean ± the standard error of the mean (n = 40 cells for each construct). **, $P < 0.01$; ***, $P < 0.001$. (C) Protein expression levels of EGFP (negative control), EGFP-Solo, EGFP–Solo-AE, and EGFP–Solo-TM(−) constructs were analyzed by Western blotting (8 μg protein per lane) with anti-Living Colors A.v. for EGFP detection. β-Actin expression was monitored as an internal control. (D to G) Effect of Solo/Trio8 on endocytosis. COS-7 cells expressing EGFP or EGFP-Solo were